UNIVERSITY OF HELSINKI REPORT SERIES IN PHYSICS

HU-P-D268

Molecular dynamics simulation of ripple formation and propagation

Alvaro Lopez-Cazalilla

Division of Materials Physics
Department of Physics
Faculty of Science
University of Helsinki
Helsinki, Finland

ACADEMIC DISSERTATION

To be presented with the permission of the Faculty of Science of University of Helsinki, for public criticism in auditorium PII of Porthania building of the University of Helsinki, on October 26 2019, at 12.00.

HELSINKI 2019

ISBN 978-951-51-2807-2 (printed version)
ISSN 0356-0961
Helsinki 2019
Unigrafia

ISBN 978-951-51-2808-9 (PDF version)
http://ethesis.helsinki.fi
Helsinki 2019
Electronic Publications @ University of Helsinki (Helsingin yliopiston verkkojulkaisut)

Alvaro Lopez-Cazalilla, **Molecular dynamics simulation of ripple formation and propagation**, University of Helsinki, 2019, **62 p.** + appendices, University of Helsinki Report Series in Physics, HU-P-D268, ISSN 0356-0961, ISBN 978-951-51-2807-2 (printed version), ISBN 978-951-51-2808-9 (PDF version)

ABSTRACT

Low and medium energy ion irradiation can induce different structures over the surface of semiconductors and metals depending on the parameters used for the irradiation of the surfaces. Different mathematical models have been developed in the last decades to explain the formation reasons of such structures, such as nano-dots or ripples, and to predict the pattern wavelength. These theories have been discussed and tested for several years. In this work, computational methods are used in order to predict and observe such effects. First, a mathematical model, which uses as an input the results from the computational methods, is applied to predict the pattern wavelength and at which angle the regime changes from stable to unstable. Moreover, a relaxation method to remove the background displacement in amorphous silicon, which affects the prediction is presented. Second, a simulation model of sequential irradiation consisting of the irradiation of a segment of the surface, and speeding-up the eventual modification of the surface is developed. The simulation outputs at ultra-low energy are compared with experimental results. The use of the same model at higher energies and applied to aluminum allows us to obtain conclusions on the reason of pattern formation in both materials at different energies and irradiation angles. The last part of this work contains the results obtained from homogeneously distributed irradiation. The irradiation is performed according to an accelerated molecular dynamics method which reduces the time span between impacts and allows us to reach higher fluences. This latter method allowed us to observe the direct ripple-formation and the propagation of the pattern on the surface for the first time. This study allows to explain and observe the different stages before the eventual ripple formation.

Contents

1 INTRODUCTION

The ion beam nano-patterning effect is the formation of a sequence of ordered structures on surfaces of solids. The wavelength and amplitude of the emerging pattern change depending on the parameters of irradiation and the material involved in the process. The nano-patterning appears to be similar to formation of sand dunes when the wind blows. The strength of the wind and the mass of the grain in the sand, among others, will determine the separation between the crests (wavelength) and the height of the formed mounds (amplitude) [1–4]. The reasons of formation of these structures in sand are highly dependent on erosion and re-deposition, however in the nano-scale in addition to these effects, we may need to take into account other atomic processes, e.g. stress build-up.

The use of ion beams to modify the surface of semiconductors offers a promising way to assist in manufacturing process of nanostructured devices, which in many cases need well-ordered regular structures [5]. The periodic structures can go from quantum dots to ripples depending on the irradiation conditions [6–9]. The critical angle (θ_c) defines the observation of the nanopatterns, i.e. below that angle (toward normal incidence) the observation of these effects is not possible. This occurs because of the stability of the surface, which suppresses the re-organization of the surface, leaving the surface flat. On the other hand, if the incidence angle is greater (toward grazing incidence) than θ_c, the surface becomes unstable and the conditions will be favourable to the observation of nanopatterns. The orientation of these patterns is characterized by the dominant wave vector. If this is parallel to the ion beam projection, the orientation of the ripples will be aligned with the ion-beam-projection. If, on the contrary, the wave vector is perpendicular to the projection of the ion beam, the ripples will be perpendicular. Typically the perpendicular-oriented formation occurs at grazing incidence [10, 11]. In FIG. 1 we can observe how for a given energy, the orientation of the ripple changes as a function of the irradiation angle.

In FIG. 2, we see how the selection of different energies and irradiation angles for Ar ions provokes the Si surface to ripple either parallel or perpendicular to the projected ion beam direction. Below a certain angle, the surface remains flat.

Ion beam sputtering (IBS) is a well-established technique to obtain the formation of self-organized structures on the surface. Originally, in 1960 Cunningham et al. [13] observed that when irradiating different metals at 70^o off-normal with various noble gases, the case of 8 keV-Ar^+ over gold was the only one that showed self-organization on the surface. Navez et al. [14] in 1962 showed that they could produce parallel and perpendicular mode ripples. Many theories have been developed during the last years, based on different effects such as the sputtering-curvature or the atomic redistribution. Sigmund [15] stated that the pattern formation induced by IBS was caused by the dependence of the sputtering yield with the surface curvature and, the number of sputtered atoms is proportional to the energy deposited on the surface of the material.

Bradley and Harper [16] proposed a theory known as Bradley-Harper (BH) theory. This theory is based on the effect created by the erosion (sputtering) in the surface. The

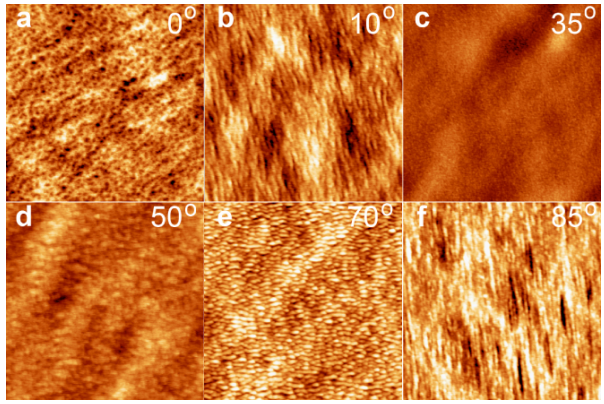

Figure 1: Effect of incidence angle on surface morphology following irradiation with 250 eV Ar^+ on Si at room temperature. AFM images of 2 μm $\times$ 2 μm scan size for (a) 0°, $3.8\times10^{18}Ar^+$ cm^{-2} (18 min), vertical range 3.5 nm, (b) 10°, 18 min, vertical range 3 nm and (c) 35°, 18 min, vertical range 3 nm. A scan size of 1 μm $\times$ 1 μm for (d) 50°, $3.2\times10^{17}Ar^+$ cm^{-2} (90 s), vertical range 2 nm (e) 70°, 90 s, vertical range 3.5 nm (parallel mode ripples) and (f) 80°, 90 s, vertical range 3.5 nm (perpendicular mode ripples). The irradiation direction goes from the bottom of the page. From [10].

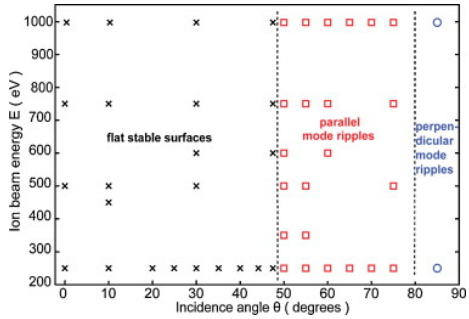

Figure 2: Phase diagram of pattern formation of Ar^+ ion beam sputtering of nominally room temperature Si(001) in the linear regime of surface dynamics, in the absence of secondary scattering effects. Crosses: flat; square: parallel mode ripples; circle: perpendicular mode ripples. Fluence is 3.8 $\times$ 10^{18} Ar^+ cm^{-2} for flat stable surfaces and 3.2 $\times$ 10^{17} Ar^+ cm^{-2} for parallel and perpendicular mode ripples. The critical angle is at $\theta \approx 50°$. From [12].

development of this theory is based on the local angle of incidence of the ion, meaning that the curvature of the surface is playing an important role, since the energy deposited on the material is different whether the surface is either convex or concave.

Later in the 1990's, Carter and Vyshniakov [17] proposed that an atomic flux is created in the direction of the ion beam projection, and this can compensate the curvature-dependent sputtering process at close-to-normal incident angle, while at a larger angle, the rippling effect can take place. Besides, they proposed that a competition between the sputtering and the irradiation-induced surface relaxation at oblique-incidence irradiation is the cause of the surface ripple formation. Essentially, the inclusion of the ballistic

diffusive term gave an important role in the formation of nanostructures, predicting that mass redistribution is determinant to the stability of the surface. This contribution has been analyzed experimentally [18].

In 2009, Norris et al. [19] described a mathematical model which was developed to understand and quantify the reasons of the nanopatterning formation. The erosion rate which takes place during the bombardment process can be divided in two terms, a long term and short term contribution. Norris et al. introduced a mathematical model to describe the sputtering and displacement effects taking place during the first picoseconds of the process. This model determines each contribution using as input computational methods such as molecular dynamics (MD) or binary collisions approximation (BCA). This model was able to estimate nanopatterns wavelength with reasonably good agreement with experimental results [20] [Publication **II**, Publication **I**].

At the beginning of 2000's [22] and in 2010's [23–25], the role of the build-up stress was analyzed and linked to the formation of ripple in surfaces.

A new MD set-up simulation was developed to observe a fast effect on the surface [Publication **II**, Publication **IV**], reducing the impact area (linearly focused), reaching high fluences and inducing a more rapid change in the surface. This type of simulation allows to observe whether is possible to observe surface modification[Publication **II**], and, at different energies and irradiation angles, test the difference between materials [Publication **IV**].

A new model was introduced [Publication **III**] which can reproduce the nanopatterning effect for ultra-low energy Ar irradiation on Silicon taking into consideration the effect of mass redistribution within the material.

2 PURPOSE AND STRUCTURE

The purpose of this work is to predict the pattern formation and develop a method to observe the formation of ripples over surfaces, by means of computational methods. The models developed in this thesis provides useful tools for the analysis of surfaces effects.

The thesis comprises a brief summary of the work and four original articles already published or submitted for publication in different international peer-review journals. The publications are included as an appendix in the dissertation and referred to with bold Roman numbers in the text.

The structure of the thesis is as follows: in this section a summary of the publications is done, and also other scientific contributions of the author are presented. In Section 3 we show the different theories developed in the field based on the different effects observed in order to explain the ripple formation. In Section 4, we introduce the basis of MD and the role that it took in the work presented in this thesis, as well as the analysis perfomed in order to get the desired results. In Section 6, we discuss how the irradiation of surfaces is done experimentally and describe the observation methods of more extended use to study the nano-patterning effect. In Sections 7 and 8, we analyse the results in which this thesis is based. In Section 9, we summarize the work included in this thesis and following this, the acknowledgement and references can be found. At the end, all the publications are attached.

2.1 Summaries of publications

Publication I: Simulation of redistributive and erosive effects in a-Si under Ar^+ irradiation

A. Lopez-Cazalilla, A. Ilinov, L. Bukonte, K. Nordlund, F. Djurabekova, S. Norris, J.C. Perkinson: Nuclear Inst. and Methods in Physics Research B 414 (2018) 133-140

In this publication, the comparison between molecular dynamics (MD) and binary collisions approximation (BCA) is performed for predicting the wavelength of 250 and 1000 eV Ar^+ on a-Si using the crater function formalism. The results showed that, due to the small displacements which BCA does not consider, MD is a more accurate method to estimate the nanopattern wavelengths.

Publication II: Pattern formation on ion-irradiated Si surface at energies where sputtering is negligible

A. Lopez-Cazalilla, D. Chowdhury, A. Ilinov, S. Mondal, P. Barman, S. R. Bhattacharyya, D. Ghose, F. Djurabekova, K. Nordlund and S. Norris: J. Appl. Phys., Vol. 123, p.

235108 (2018)

We introduce a new method to simulate the nanopatterning effect consisting of the irradiation of a segment of a cell, which allows us to reproduce experimental fluences. The simulations with the focused method, along with the single-ion irradiation analyzed with the crater function formalism, give a good prediction of the experimentally observed surface rippling.

Publication III: Direct observation and propagation of ripples under low energy Ar irradiation

A. Lopez-Cazalilla, F. Djurabekova and A. Ilinov, C. Fridlund, K. Nordlund (2019) (submitted for publication)

By using a novel accelerated molecular dynamics methodology, we are able to simulate directly the process of ripple formation by high fluence ion irradiation. Since this approach neither requires a precursor nor pre-assumes a mechanism to trigger self-organization, it can provide first-principles insight into the origin of the ion-induced ripple formation mechanism. Analysis of the simulation shows the exact mechanism of the process, which is dominated by surface atom displacement and a pile-up effect.

Publication IV: Modeling of high-fluence irradiation of amorphous Si and crystalline Al by linearly focused Ar ions

A. Lopez-Cazalilla, A. Ilinov, K. Nordlund and F. Djurabekova: Journal of Physics: Condensed Matter, Vol. 31, Num. 7, p. 075302 (2019)

In this work we analyse under the same circumstances two materials, silicon (amorphous) and aluminium (crystalline), putting special attention to the 70° off-normal irradiation. We show that atomic redistribution mechanism is the driving force for ripple formation in the amorphous material (silicon) and, on the other hand, erosion mechanism is the main contributor to the pattern formation in crystalline metals (aluminium).

2.2 Author's contribution

The author performed all the simulations included in [Publication **I**] [Publication **II**] [Publication **III**] [Publication **IV**]. Christoffer Fridlund developed the method used in [Publication **III**] (from [28]) and wrote the first versions of the used scripts. Information about the stress accumulation in Si was provided by Joy Perkinson in her doctoral dissertation.

The author wrote the first version of all manuscripts.

3 THEORY OF RIPPLE FORMATION

3.1 Sputtering

The erosion or sputtering was early assumed to be the main explanation for nanopattern formation. Sigmund developed a model to explain the dependence of the sputtering yield on the surface curvature [15, 29], which is related to the deposited energy in the system described by a Gaussian function. A random point in the solid $\mathbf{r} = (x, y, z)$ is defined fulfilling $z \leq h(x, y)$. The function h is the height of the surface z = h(x, y). The deposited energy at a point $\mathbf{r}$ is defined as follows,

$$F_D(\mathbf{r}) = \frac{\epsilon}{(2\pi)^{3/2}\alpha\beta^2} \times \exp\left[-\frac{[z - h(0,0) + a]^2}{2\alpha^2} - \frac{x^2 + y^2}{2\beta^2} \right], \tag{1}$$

where ϵ is the total deposited energy, a is the average depth of the energy deposited in the material, and α and β are the longitudinal and lateral widths of the distribution.

Later Bradley and Harper [16], based on Sigmund's work, created a theory based on the dependence of the sputtering yield on the surface curvature, which was determined in order to measure the deposited energies in the system. It was the first study which, based on erosive effect, found an explanation for the periodic formations observed experimentally and modelled it. The developed theory failed to predict the surface erosion at grazing incidence: in this model, the sputtering yield over an unperturbed surface is continuously increasing, even at high incidence angle, an effect that is not happening experimentally. The curvature of the surface plays an important role in the energy deposition in the system, which is the reason of taking into account this variable in the erosion calculation. Furthermore, the energy deposited on a concave surface to the solid is greater than that deposited in a convex, hence the velocity of the surface at a certain point in the surface due to erosion needs to be defined based on the curvature coefficients:

$$v(\theta, c_1, c_2) = (f/n)Y_0(\theta)[\cos(\theta) - \Gamma_x(\theta)a\frac{\partial^2 h}{\partial x^2}(0,0) - \Gamma_y(\theta)a\frac{\partial^2 h}{\partial y^2}(0,0)]. \tag{2}$$

Here θ is the irradiation angle, f is the flux, n is the number of atoms per unit volume, $\mathrm{Y_0}(\theta)$ is the sputtering yield in the condition of a flat surface, and $\Gamma_\mathrm{x}(\theta)$ and $\Gamma_\mathrm{y}(\theta)$ are the coefficients which govern the erosion rate of the surface. Hence, the change of the surface height is defined using the following PDE as a Taylor expansion of the velocity of the surface,

$$\frac{\partial h}{\partial t} \approx -v_0(\theta) + v_0'(\theta)\frac{\partial h}{\partial x} + \Gamma_x(\theta)\frac{\partial^2 h}{\partial x^2} + \Gamma_y(\theta)\frac{\partial^2 h}{\partial y^2} - B\nabla^2(\nabla^2 h), \tag{3}$$

where $\mathrm{v_0}(\theta)$ is the rate of erosion of the unperturbed planar surface, $\mathrm{v_0'}(\theta)$ is the first derivative of the rate of erosion and $\mathrm{B}\nabla^2(\nabla^2\mathrm{h})$ describes the surface self-diffusion. After the BH theory, many expansions and generalizations have been published [30–33] in which

non-linear terms were included in the PDE describing the change of the surface height from the Kardar-Parisi-Zhang (KPZ) equation [34]:

$$\frac{\partial h}{\partial t} = -v_0(\theta) + v_0'(\theta)\frac{\partial h}{\partial x} + \Gamma_x(\theta)\frac{\partial^2 h}{\partial x^2} + \Gamma_y(\theta)\frac{\partial^2 h}{\partial y^2} + \frac{\lambda_x}{2}\left(\frac{\partial h}{\partial x}\right)^2 + \frac{\lambda_y}{2}\left(\frac{\partial h}{\partial y}\right)^2 - B\nabla^2(\nabla^2 h) + \eta(x,y,t), \tag{4}$$

where λ_x and λ_y are the coefficients characterizing the slope dependence of the erosion rate [31] accompanying terms which include the interface growth or its erosion ($(\partial h/\partial x)^2$ and $(\partial h/\partial y)^2$), η describes the stochastic incoming ions represented by the Gaussian white noise. Under some approximations, e.g. neglecting the non-linear terms, many experiments have been explained using this theory [5, 35].

In the described theories the redistribution was not included to describe the irradiation-induced effects. In the next section theories including this driving force are discussed.

3.2 Displacement

The introduction of the BH theory gave the first reasonable explanation of the pattern formation. However, many studies came later based on the Carter-Vishnyakov (CV) model [17], which took into consideration more variables for the pattern formation field. The effect of the surface diffusion or the induced displacement as a driving force were introduced as an additional explanation for the pattern formation. The incident ions transfer momentum to the atoms, the induced displacements close to the surface are in the perpendicular direction to the trajectory of the ion, but deeper they are parallel to the ion direction. Hence, at normal incidence, the atoms are displaced in a balanced way along the parallel and perpendicular direction to the ion beam projection, inducing the effective ballistic diffusivity. On the other hand, at off-normal incidence, the balance breaks, and an effective atomic drift parallel to the surface takes place. The CV model suggested that under certain conditions [17], the ballistic displacement and the effective diffusivity can be dominant in the surface relaxation mechanism. However, at higher temperature, thermal diffusion can have a more important role. The combination of the mentioned ballistic diffusion and the ballistic displacement effect could give an explanation to the non-rippling effect at close-to-normal incidence.

The schematic shown in FIG. 3 summarizes the different approaches introduced once the atomic displacement was taken into consideration.

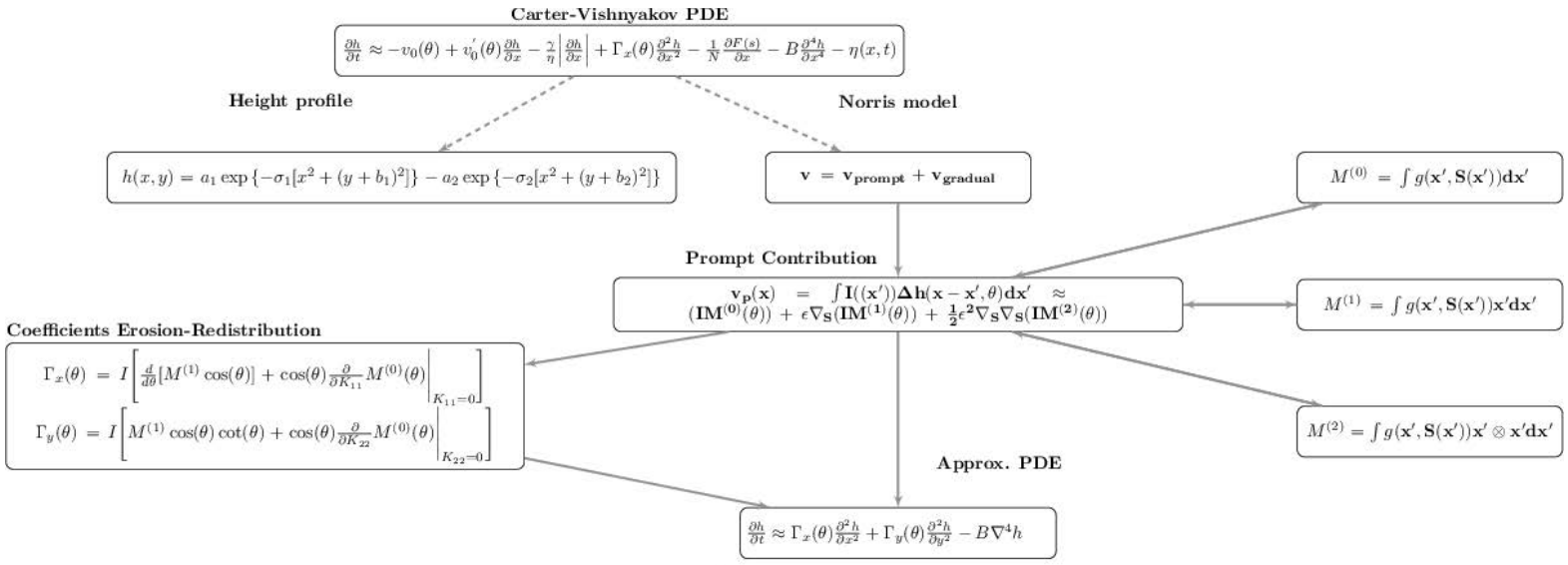

Figure 3: Evolution of the different approaches to describe the surface evolution.

Hence, Carter and Vishnyakov introduced two terms into the PDE introduced by Bradley and Harper [16] (in this case expressed in the x-z plane),

$$\frac{\partial h}{\partial t} = -v_0(\theta) + v_0'(\theta)\frac{\partial h}{\partial x} - \frac{\gamma}{\eta}\left|\frac{\partial h}{\partial x}\right| + \Gamma_x(\theta)\frac{\partial^2 h}{\partial x^2} - \frac{1}{N}\frac{\partial F(s)}{\partial x} - B\frac{\partial^4 h}{\partial x^4} - \eta(x,t), \quad (5)$$

where the terms introduced are $\gamma/\eta|\partial \mathrm{h}/\partial \mathrm{x}|$, which takes into account the viscous relaxation effects [35] (where γ and η are the surface free energy density and the viscosity, respectively), $\eta(\mathrm{x},\mathrm{t})$, which is the noise and the term $\frac{1}{\mathrm{N}}\frac{\partial \mathrm{F(s)}}{\partial \mathrm{x}}$ illustrates the influence of the gradient of an atomic flux F(s) parallel to the surface.

Starting with the CV model, the atomic displacement took an important role in the pattern formation theories. Kalyanasundaram et al. [36] presented a work which introduced the study of the *crater function* ($\Delta h(\mathbf{x}-\mathbf{x_0},\theta)$) using MD [37], where a crystalline Si sample containing 8000 atoms was irradiated using 500 eV and 700 eV Ar^+ ions at 77 K. The sample was irradiated from normal to 28°, and then, obtaining some parameters averaging the data over 500 to 2000 single impacts, an equation was fitted to determine the height modification.

$$h(x,y) = a_1 \exp\{-\sigma_1[x^2+(y+b_1)^2]\} - a_2 \exp\{-\sigma_2[x^2+(y+b_2)^2]\}, \quad (6)$$

where $\mathrm{h}(\mathrm{x},\mathrm{y})$ is the height of the surface at the point (x,y) of the surface, x being the projected direction of the incoming ion, and y the perpendicular distance relative to the point of impact. The rest are fitting constants presented in [36]. The results showed that the crater created was not only a product of the sputtering, because sputtering only created approximately 20% of the volume. Hence, the atomic redistribution was something worth considering in the ripple formation.

After that work, a model was proposed to determine the ripple formation using MD also using single impacts, in which the continuum models proposed so far were treated according to a new formalism. The model proposed by Norris et al. [19] separates the erosion rate in two effects: the *prompt* (v_p) and the *gradual* (v_g). This model predicts the pattern wavelength based on the so-called *prompt effect*, which considers the effects taking place during the first picoseconds, while the effects that happen at longer times are accounted in the *gradual* part. The v_p can be analyzed using either MD or BCA, and accounts for the crater function, which describes the change of the surface. The main part of interest is the atomic redistribution, since it came up to be discussed in the surface pattern formation later than erosion, and finding a way to relate the microscopic effect with the eventual macroscopic formation.

The crater function defined as $g = \Delta h$ is used to describe the surface evolution as follows,

$$v_p(\boldsymbol{x}) = \int I((\boldsymbol{x'}))\Delta h(\boldsymbol{x}-\boldsymbol{x'},\theta)d\boldsymbol{x'}, \quad (7)$$

where $\mathrm{I}((\mathbf{x}'))$ is the flux, $\mathbf{x}'$ is a point in the tangent plane to the surface at $\mathbf{x}$ and the crater function Δh is based on the average local change of the surface at that certain

point $\mathbf{x}$ due to single impact in $\mathbf{x}'$ (local coordinates, respect to the impact point) and its consecutive derivatives. Besides, considering the surface evolution, it can be expressed in terms of the moments of the crater function [20],

$$v_p(\boldsymbol{x}) = (IM^{(0)}(\theta)) + \epsilon\nabla_{\boldsymbol{S}}(IM^{(1)}(\theta)) + \frac{1}{2}\epsilon^2\nabla_{\boldsymbol{S}}\nabla_{\boldsymbol{S}}(IM^{(2)}(\theta)) + ..., \tag{8}$$

where I is again the flux, $\nabla_{\boldsymbol{S}}$ is the surface divergence, ϵ is a small parameter connected to the ratio between the scales of the impact and the pattern formation, and the different $\mathrm{M}^{(\mathrm{i})}(\theta)$ are the moments of the crater function represented by tensors. The moments are defined as follows,

$$\begin{aligned} M^{(0)} &= \int g(\boldsymbol{x'}, S(\boldsymbol{x'}))d\boldsymbol{x'} \\ M^{(1)} &= \int g(\boldsymbol{x'}, S(\boldsymbol{x'}))\boldsymbol{x'}d\boldsymbol{x'} \\ M^{(2)} &= \int g(\boldsymbol{x'}, S(\boldsymbol{x'}))\boldsymbol{x'}\otimes\boldsymbol{x'}d\boldsymbol{x'} \\ &... \end{aligned} \tag{9}$$

where S is the parametric dependence on the surface at the point $\boldsymbol{x'}$. In Section 4.3.1, those moments are approximated in order to use single-impact simulations to calculate them [19]. Those moments are independently calculated for accounting the erosion and redistribution, and then, introduced in the linearized eq. 4 for prompt effects,

$$\frac{\partial h}{\partial t} \approx \Gamma_x(\theta)\frac{\partial^2 h}{\partial x^2} + \Gamma_y(\theta)\frac{\partial^2 h}{\partial y^2} - B\nabla^4 h, \tag{10}$$

where the coefficients are calculated as follows [38],

$$\begin{aligned} \Gamma_x(\theta) &= I\left[\frac{d}{d\theta}[M^{(1)}\cos(\theta)] + \cos(\theta)\frac{\partial}{\partial K_{11}}M^{(0)}(\theta)\bigg|_{K_{11}=0}\right] \\ \Gamma_y(\theta) &= I\left[M^{(1)}\cos(\theta)\cot(\theta) + \cos(\theta)\frac{\partial}{\partial K_{22}}M^{(0)}(\theta)\bigg|_{K_{22}=0}\right], \end{aligned} \tag{11}$$

where $K_{11} = \frac{\partial^2 h}{\partial x^2}(0,0)$ and $K_{22} = \frac{\partial^2 h}{\partial y^2}(0,0)$. The second part on the right side of both equations in eq. 11 is a term included in PyCraters [39] which is connected with the Sigmund ellipsoidal model [15]. Several works [40–42] revealed that the terms related to from-flat surface were not sufficient to analyze the pattern formation [43]. Because of that, the term related to the Sigmund model was included in the prediction (eq. 11). An important conclusion can be obtained of those studies: under certain circumstances regarding for instance to the ion energy or the subtrate, the erosion is playing a secondary role in the pattern formation [20, 40, 41].

The coefficients shown in eq. 11 are calculated in [Publication **I**] and [Publication **II**] using as an input the moments calculated from either BCA or MD. This truncated version of the PDE (eq. 10) works reasonably well in order to predict pattern formation from single-impact irradiation as was shown in [20] and [Publication **II**, Publication **I**], but the inclusion of non-linear terms helps to get a more accurate prediction [38].

Those coefficients in eq. 11 describe the stability of the surface, hence in the region where they are negative, the unstable regime starts, typically around 45° off-normal [41, 44] depending on the energy and material involved, and the conditions are favorable to observe pattern formation.

Lately, the use of new theories [23, 24] and schemes of simulation [25] have been implemented in order to study the pattern formation where, observing the evolution of the accumulation of stress, the pattern wavelength can be predicted. Along the same lines, mimicking the focused ion beam experiments, the sequential simulations [Publication **II**, Publication **IV**] where a certain number of consecutive impacts take place over a delimited region of a cell, enhancing the probability of observing any change in the surface. A newer scheme has been applied as was described in [28], where the time between impacts is reduced and after a certain number of impacts, the irradiated cell is relaxed and the initial temperature is restored. This method was successfully applied in [Publication **III**].

4 MOLECULAR DYNAMICS

In this section we describe the basics of MD, explaining how the equations which rule the atomic interactions are described computationally. MD [45, 46] is a computational method which integrates Newton's equations of motion:

$$\vec{F}_i = m_i \vec{a}_i, i = 1, 2, ..., N_{atoms}, \tag{12}$$

where m_i is the mass of the atom i in the system, and $\vec{a}_i$ is the acceleration in the three directions (x, y, z) of the atom i.

In FIG. 4 we see how the MD algorithm works.

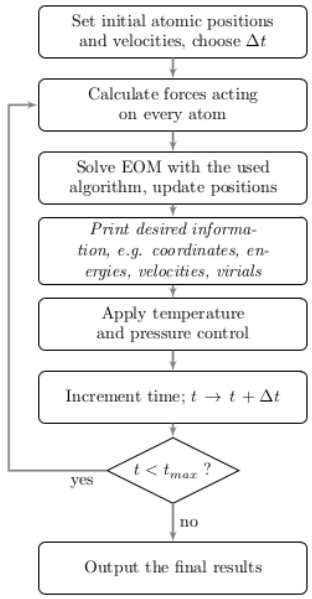

Figure 4: Diagram of how MD algorithm works. EOM stands for "equations of motion".

Starting from an initial set of positions and velocities, and a definition of the time step, the equations are integrated based on a determined algorithm. Out of the methods developed, we present here the Verlet [47, 48] and Gear predictor-corrector method [49].

In the Verlet algorithm, the Taylor series expansion is applied to the position $\vec{r}_i(t + \Delta t)$ and $\vec{r}_i(t - \Delta t)$ in the timestep after and before the current one:

$$\begin{aligned}\vec{r}_i(t+\Delta t) &= \vec{r}_i(t) + \Delta t\frac{d\vec{r}_i(t)}{dt} + \frac{\Delta t^2}{2!}\frac{d^2\vec{r}_i(t)}{dt^2} + \frac{\Delta t^3}{3!}\frac{d^3\vec{r}_i(t)}{dt^3} + O(\Delta t^4)\\ \vec{r}_i(t-\Delta t) &= \vec{r}_i(t) - \Delta t\frac{d\vec{r}_i(t)}{dt} + \frac{\Delta t^2}{2!}\frac{d^2\vec{r}_i(t)}{dt^2} - \frac{\Delta t^3}{3!}\frac{d^3\vec{r}_i(t)}{dt^3} + O(\Delta t^4)\end{aligned} \tag{13}$$

Summing these two equations up and substituting $\frac{F_i(t)}{m_i} = \frac{d^2\vec{r}_i(t)}{dt^2} = a_i(t)$, we get the value of the value for the position in the next step:

$$\vec{r}_i(t+\Delta t) = 2\vec{r}_i(t) - \vec{r}_i(t-\Delta t) + \frac{\Delta t^2}{m_i}F_i(t) + O(\Delta t^4). \tag{14}$$

There are other variations of the algorithm in order to obtain the velocities. The Gear algorithm, first, predicts a configuration of the position and its sequential derivatives of the next timestep using the Taylor series expansion,

$$\begin{aligned}{}^p\vec{r}_i(t+\Delta t) &= \vec{r}_i(t) + \Delta t\vec{v}_i(t) + \frac{\Delta t^2}{2!}\vec{a}_i(t) + \frac{\Delta t^3}{3!}\vec{b}_i(t) + \frac{\Delta t^4}{4!}\vec{c}_i(t) + \frac{\Delta t^5}{5!}\vec{d}_i(t) + O(\Delta t^6)\\ {}^p\vec{v}_i(t+\Delta t) &= \vec{v}_i(t) + \Delta t\vec{a}_i(t) + \frac{\Delta t^2}{2!}\vec{b}_i(t) + \frac{\Delta t^3}{3!}\vec{c}_i(t) + \frac{\Delta t^4}{4!}\vec{d}_i(t)\\ {}^p\vec{a}_i(t+\Delta t) &= \vec{a}_i(t) + \Delta t\vec{b}_i(t) + \frac{\Delta t^2}{2!}\vec{c}_i(t) + \frac{\Delta t^3}{3!}\vec{d}_i(t)\\ {}^p\vec{b}_i(t+\Delta t) &= \vec{b}_i(t) + \Delta t\vec{c}_i(t) + \frac{\Delta t^2}{2!}\vec{d}_i(t)\\ {}^p\vec{c}_i(t+\Delta t) &= \vec{c}_i(t) + \Delta t\vec{d}_i(t)\\ {}^p\vec{d}_i(t+\Delta t) &= \vec{d}_i(t),\end{aligned} \tag{15}$$

where the superscript p stands for predicted, $\vec{r}_i$ is the position of the atom i, $\vec{v}_i$ is the velocity, $\vec{a}_i$ is the acceleration and $\vec{b}_i$, $\vec{c}_i$ and $\vec{d}_i$ are consecutive derivatives of the position. Then, the forces are evaluated using the interatomic potential for the $t + \Delta t$ step, and using the difference between this calculation and that predicted in eq. 15, gives us the correction,

$$\Delta\vec{a}_i(t+\Delta t) = \vec{F}_i(t+\Delta t)/m_i - {}^p\vec{a}_i(t+\Delta t). \tag{16}$$

This difference is applied to correct the prediction already done,

$$\begin{aligned}{}^c\vec{r}_i(t+\Delta t) &= {}^p\vec{r}_i(t+\Delta t) + \alpha_0\Delta\vec{a}_i\\ {}^c\vec{v}_i(t+\Delta t) &= {}^p\vec{v}_i(t+\Delta t) + \alpha_1\Delta\vec{a}_i\\ {}^c\vec{a}_i(t+\Delta t) &= {}^p\vec{a}_i(t+\Delta t) + \alpha_2\Delta\vec{a}_i\\ {}^c\vec{b}_i(t+\Delta t) &= {}^p\vec{b}_i(t+\Delta t) + \alpha_3\Delta\vec{a}_i\\ {}^c\vec{c}_i(t+\Delta t) &= {}^p\vec{c}_i(t+\Delta t) + \alpha_4\Delta\vec{a}_i\\ {}^c\vec{d}_i(t+\Delta t) &= {}^p\vec{d}_i(t+\Delta t) + \alpha_5\Delta\vec{a}_i,\end{aligned} \tag{17}$$

where c stands for corrected, and the coefficients α_{i} are those on which the stability of the algorithm depends on. Also a list of neighbours based on the radius which defines the number of atoms is used to determine how many atoms we take into consideration to calculate the desired information. In the PARCAS MD code [50] the Gear algorithm, which is quite convenient for applying pressure and temperature rescaling, is used.

The use of an interatomic potential is needed to describe the interaction between the atoms in the system. Besides, when needed, a control over the temperature and pressure is used. These controls are done using different methods. Some common ways are the Berendsen [51] and Nosé-Hoover [52] thermostats and barostats. In this work only the Berendsen thermostat and barostat are used when are needed in the simulations. The λ and μ factor are used to rescale the temperature and pressure, respectively, and these are defined as follows,

$$\begin{aligned} \lambda &= \sqrt{1 + \frac{\Delta t}{\tau_T}\Big(\frac{T_0}{T(t)} - 1\Big)} \\ \mu &= \left[1 + \frac{\beta \Delta t}{\tau_P}(P(t) - P_0)\right]^{1/3}, \end{aligned} \tag{18}$$

where Δt is the defined timestep, β is the inverse of the bulk modulus, τ_{T} and τ_{P} are the time constants of the algorithm giving the scaling rate, T_0 and P_0 are the aimed temperature and pressure, respectively, and T(t) and P(t) are the instantaneous temperature and pressure, respectively. The two time constants are related to T(t) and P(t) in the following way,

$$\begin{aligned} \frac{dT(t)}{dt} &= \frac{T_0 - T(t)}{\tau_T} \\ \frac{dP(t)}{dt} &= \frac{P_0 - P(t)}{\tau_P}, \end{aligned} \tag{19}$$

where as a function of time, the temperature and pressure of the system converge to the defined temperature and pressure exponentially in the defined thermal bath region. Then, using this thermal bath coupling, the velocities and volume are scaled when this algorithm is on.

4.1 MD of irradiation effects

In order to irradiate the surface object of the study, we need to place the ion at a certain distance from the surface with the desired energy. The impact point will be described by the initial position and the incident (polar) angle (θ) and the azimuthal angle (φ). Once the ion starts its path towards the surface, at a certain distance set by the potential cutoff radius, it starts to interact with atoms in the surface and, as a function of the initial energy and the incidence angle, the induced effect in the surface varies. As the irradiation angle increases (at fixed energy), the probability of penetration of the ion in the material decreases, since at grazing incidence it is more probable for the ion to be reflected.

The description of the interaction between the ion and the material is done based on the concept of stopping power [53], i.e. as the ion penetrates the material, it loses energy. The stopping power is defined as the amount of energy that a charged particle loses as a function of the covered distance. Hence we describe it as follows,

$$S(E) = S_{nuclear}(E) + S_{electronic}(E) = -\Big(\frac{dE}{dr}\Big)_{nuclear} - \Big(\frac{dE}{dr}\Big)_{electronic}, \tag{20}$$

which is the sum of two contributions: nuclear and electronic. The nuclear, which is dominant at low energies (below 100 keV), is pure elastic interactions of the ion with other nuclei in the system; and the latter, at higher energies, inelastic interactions with the electronic systems of the atoms in the system. A schematic vision of the dependence of the stopping power on the ion energy is shown in FIG. 5,

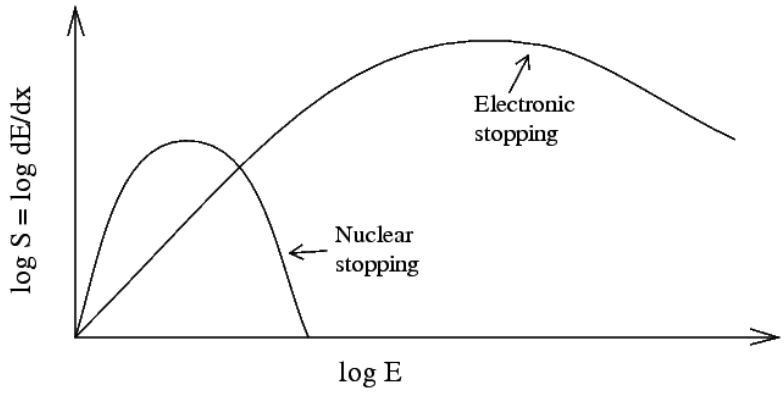

Figure 5: Electronic and nuclear stopping power. Typically, below 100 keV the nuclear stopping power is dominant. For MeV energies the electronic stopping power is dominant [53].

In MD, the nuclear stopping power is calculated directly, since it is purely nuclear interactions ($S_{nuclear}(E)$) which are governed by the repulsive Coulomb forces. Hence, when a

projectile having a mass of m_1 and kinetic energy E interacts with an atom of mass m_2, the transmitted energy (E_t) can be calculated as follows [54],

$$E_t = 4\frac{m_1 m_2}{m_1 + m_2} E\cos(\theta), \tag{21}$$

where θ is the scattering angle. Hence, this energy will play a role in the nuclear stopping power through the scattering cross section $\sigma(E, E_t)$. Considering this, we can calculate $S_{nuclear}(E)$ as:

$$S_{nuclear}(E) = -\frac{dE}{dr} = N\int_{E_t^{min}}^{E_t^{max}} E_t\sigma(E, E_t)dE_t, \tag{22}$$

where N is the atomic density of the target material.

The electronic part ($S_{electronic}(E)$) is more relevant for energetic projectiles. In MD, $S_{electronic}(E)$ is included as an external function [55], usually implemented as a frictional force [56]. When the ion energy is high, as can be seen in FIG. 5, the stopping power is dominated by the electronic stopping power, and as the ion starts to lose energy, the nuclear stopping power becomes more important.

4.2 Making stable a-Si and c-Al structures

In this section we explain how the structures used for generating the different results were created in order to provide reliable results on the surface effect analysis. We created three different cells (two of silicon and one of aluminium) to perform the same kind of simulations but for different energies.

In order to describe the interaction between the Si atoms in the material we used the environment-dependent inter-atomic potential (EDIP) [57, 58] which was complemented by the pure repulsive Ziegler-Biersack-Littmark (ZBL) [55] potential at short distances [59]. The EDIP describes a-Si well as well as the melting point [60].

The Al-Al interactions were described using the embedded-atom method (EAM) potential [61] for Al [62] joined to the repulsive ZBL [55] potential, fine-tuned in order to give the correct values of the threshold displacement energy [63].

4.2.1 Large size a-Si cell

In order to perform 250 and 1000 eV Ar^+ irradiation, we need to relax the sample enough to obtain the most reliable results. The initial structure was a $10 \times 10 \times 10$ nm^3 cell with periodic boundary conditions in the three directions. The Wooten-Winer-Weaire (WWW) method was applied [64] to that cell in order to get an amorphous structure needed for the study, since this method provides an optimized structure obtaining a coordination number of 4 for most of the Si atoms. The cell was replicated in order to obtain the cell used in [20], because the WWW method is computationally too expensive to apply in larger samples. The resulting sample is $40 \times 40 \times 10$ nm^3. This cell was then equilibrated at 300 K using Berendsen temperature and pressure control [51] to reduce the internal stress using a time constant equal to 500 ps. After this process, the size of the system was fixed and the system was annealed at 1000 K and linearly cooled down to 300 K sequentially 20 times during 50 ps.

Since we wanted to simulate higher energies than the ones simulated in the previous work [20, 65], the cell was replicated 3 times in the x direction for more realistic cooling conditions and to avoid possible shock waves as a product of the impacts. The surface in the z direction was opened, leaving the periodic conditions in the x-y plane, and the system was relaxed during 50 ps at 300 K.

The target temperature for the analysis we needed to perform was 0 K. The reason is that at that temperature, we are able extract the purest effect of the displacement field. Therefore, the cell was taken to $\approx$0.001 K using the Berendsen thermostat[51] for 15 ps. The last relaxation helped to remove the background displacement which causes misleading results, as reported in [20]. The resulting cell was used to perform the single ion Ar^+ irradiation.

4.2.2 Small size a-Si cell

The cell used for the sequential irradiation in [Publication **II**], [Publication **III**] and [Publication **IV**] was extracted from the original cell developed in [Publication **I**] and described in Section 4.2.1. The size of the cell is enough to encase a complete cascade at energies similar to the ones simulated in the performed work. To perform the consecutive irradiation, the cell was equilibrated at 300 K. The way is explained as follows:

- The initial cell with periodic boundary conditions in the three directions was taken from 0 to 300 K applying during 100 ps the Berendsen thermostat [51].
- Then, a NPT ensemble using the Berendsen algorithm [51] was used during 50 ps at 300 K.
- At the end of the process, a 1 nm-thick layer was immobilized in order to prevent the system motion during the consecutive irradiation and the surface was opened and relaxed during 100 ps.

After the whole relaxation process, the size of the cell was $16.56 \times 16.56 \times 5.15$ nm^3 consisting in 73548 Si atoms.

Besides the sequential irradiation, this cell was used in the single ion impacts reported in [Publication **II**] However, as we did with the larger cell in Sec. 4.2.1, we carried the system to 0 K in order to obtain a better accuracy extracting the moments needed for the analysis.

4.2.3 c-Al cell

In [Publication **IV**], we compare the same effect in a-Si and c-Al in order to analyze the effect in crystal structure, so we needed a stable c-Al structure of comparable size. The face-centered-cubic (FCC) structure was created at 0 K with periodic boundaries in the three directions. The system was heated up during 10 ps to 300 K, which is the target temperature. After this, the surface in the z direction was opened and finally relaxed for another 10 ps in order to minimize the internal stresses. At the bottom of the cell, a 1 nm-thick layer was immobilized as well to prevent the system motion. The final size of the cell is $16.20 \times 16.20 \times 5.27$ nm^3 containing 83200 Al atoms.

4.3 Simulation modes for ripples

This section discloses the different types of simulations that were implemented in order to obtain the desirable results.

4.3.1 Crater function

The crater function formalism was developed by Norris et al. [19] as was explained in Section 1, for giving an explanation to the pattern formation, and, besides, measure the different contributions (erosive and redistributive) which lead to the formation process to take place. This formalism has been applied successfully in several works [20, 44] [Publication **II**, Publication **I**]. In this part of the thesis, we are interested in extraction of the moments, which allow us to determine the nanopattern wavelength, as well as the cause of formation of these ripples. In order to collect statistics, the Ar^+ ion position is selected to impact in the center of the cell on the surface, which has been previously randomly shifted in the x-y direction. This way, the impact point is always randomly selected. The Ar-Si interaction is described by the purely repulsive ZBL potential [55]. The azimuthal angle is randomly selected as well.

The simulated events for the different energies, angles and number of cases are:

1. 30 eV-Ar^+ (200 cases): 0°, 15°, 30°, 45°, 60°, 70°, 80°, 85°, 87°
2. 250 eV-Ar^+ (300 cases): 0°, 15°, 30°, 45°, 60°, 70°, 75°, 80°, 82°, 84°, 85°, 86°, 87°, 88°
3. 1000 eV-Ar^+ (600 cases): 0°, 15°, 30°, 45°, 60°, 70°, 75°, 80°, 82°, 84°, 85°, 86°, 87°, 88°

We use two a-Si cells, one of about 2.66×10^6 atoms (Sec. 4.2.1) for the 1000 eV and 250 eV single ion irradiation in [Publication **I**] and the small one of 7.3×10^4 (Sec. 4.2.2) at 30 eV [Publication **II**].

The performed simulations allowed us to extract information which could be used to extract the moments, which will determine the stability coefficients as explained in Section 3.2. These moments are defined for the erosive contribution as follows:

$$\begin{aligned} M^{(0)}_{erosive} &= -V_{Si} \sum_{j=1}^{N_{sputtered}} 1 \\ M^{(1)}_{erosive} &= -V_{Si} \sum_{j=1}^{N_{sputtered}} \boldsymbol{u}_j^{initial}, \end{aligned} \tag{23}$$

where V_{Si} is the atomic volume of Si (0.02 nm^3), $N_{sputtered}$ is the number of sputtered atoms per impact, which are found at the location above 5 Å over the surface at the

end of the simulation, and $u_j^{initial}$ represents the initial position of the sputtered atoms ($u_j^{initial} = x_j^{initial}, y_j^{initial}$). Regarding the redistributive effect, we have:

$$\begin{aligned} M_{redist.}^{(0)} &= 0 \\ M_{redist.}^{(1)} &= V_{Si} \sum_{j=1}^{N_{redistributed}} (u_j^{final} - u_j^{initial}), \end{aligned} \tag{24}$$

where $N_{redistributed}$ are these atoms which are reallocated within the system as a result of the ion impact and ($u_j^{final} = (x_j^{final}, y_j^{final})$). The $M_{redist.}^{(0)}$ is equal to zero by definition, because of the conservation of mass.

The erosive part depends on the number of sputtered atoms and their initial positions on the surface, while the change in position of the atoms contributes to the redistributive part, i.e. how much these atoms were displaced as a result of the ion impact. Since the azimuthal angle is randomly selected for every impact, we need to transform the coordinates to the local system of reference based on the surface normal and the ion beam projection direction. Hence, the coordinates used for the analysis are transformed as follows,

$$\begin{aligned} x_j &= x_j^{'} \cos(\varphi) + y_j^{'} \sin(\varphi) \\ y_j &= -x_j^{'} \sin(\varphi) + y_j^{'} \cos(\varphi), \end{aligned} \tag{25}$$

where φ is the azimuthal angle, $(x_j^{'}, y_j^{'})$ are the original coordinates of the atoms and (x_j, y_j) are the rotated coordinates of the atoms. Both the initial and final atomic coordinates should be rotated for every atom in the system.

Once the moments introduced in eqs. 23 and 24 are calculated, they can be used in Pycraters [39] and to estimate the coefficients needed to determine the stability of the surface.

The height of the surface $h(x, y, t)$ can be described in terms of the normal modes of the wave vector $\mathbf{q}$ via Fourier methods [18, 41, 66], and it is introduced as a solution of the eq. 10. Hence, the amplification rate equation can be written as follows,

$$R(\mathbf{q}) = -\Gamma_x(\theta) q_x^2 - \Gamma_y(\theta) q_y^2 - B(\theta)(q_x^2 + q_y^2)^2, \tag{26}$$

where $R(\mathbf{q})$ values are measured experimentally, $\mathbf{q}$ is the wave vector in the (x,y) direction and $B(\theta)$ is the viscous flow coefficient (used in eq. 4 and 3). The dependence of B on the irradiation angle is defined by the thickness of the amorphous layer which indeed is related to the effect of the incoming ions on the material. Initially it had been calculated as explained in the supplementary material of [20] and in [Publication **I**], considering it constant and independent of the irradiation angle. However, since the amorphous layer thickness depends on the penetration depth (which is directly dependent on the incidence

angle), we calculate the thickness as twice the penetration depth [44] (in [Publication **II**]). The penetration width was calculated using the MDRANGE code [56] for different angles and used as an input to estimate the wavelength.

The experimental measurement of R(**q**) determines that while the surface remains stable, this coefficient will be below zero. Hence, when the instability regime starts, R is zero, so from eq. 26, the wavelength in the parallel or perpendicular direction can be estimated as $\lambda_{x,y} = \frac{2\pi}{q_{x,y}}$. Having the coefficients $\Gamma_{\mathrm{x}}(\theta)$ and $\Gamma_{\mathrm{y}}(\theta)$, we can predict the ripple wavelength in the following way,

$$\lambda_{x,y} = 2\pi\sqrt{\frac{2B(\theta)}{-f\Gamma_{x,y}(\theta)}}, \tag{27}$$

where f is the ion beam flux. The direction of the wavelength is decided to be either parallel (x) or perpendicular (y) based on which one is the most negative (unstable).

Besides the analysis which is similar to the one done in [20], we incorporated first in [Publication **I**] for 250 and 1000 eV and for 30 eV in [Publication **II**] an additional calculation to the ruling coefficients $\Gamma_{\mathrm{x,y}}$. The new setting was the estimation of the confidence intervals in the $\Gamma_{\mathrm{x,y}}$ coefficients, which provides a probability of domination of one of the modes (parallel or perpendicular) for the wavelength calculation. This setting gives one σ extracted from the moments (eq. 23 and 24). The use of this setting enables for all the simulated angles the relative probability of orientation in each direction of those predicted patterns (especially important at grazing incidence). The error boundary estimations on the coefficients also allow us to provide an uncertainty in the wavelength prediction.

4.3.2 Sequential irradiation

In this subsection, the methodology used to develop the results shown in [Publication **II**] and [Publication **IV**] is discussed. Due to the limitations in time and size in simulating long-time and randomly distributed impact points on the surface, irradiating a segment is of interest. The reason is that we can reach local fluences comparable to the experimental ones, not trying to reproduce a real well ordered rippling effect, but aiming to observe how the possible surface modification occurs.

The simulated ion energies were 30, 250 and 1000 eV. The maximum number of impacts simulated is 10000 Ar^+ for 30 and 250 eV, and 4000 Ar^+ for 1000 eV for both a-Si and c-Al. The ions were located 5 Å above the surface of the cell at a certain position, and were directed toward a certain region of the cell. The chosen region is the segment consisting of a 10% width in the x direction and the full length in the y direction. After every impact, the cell is randomly shifted in the y direction and the x coordinate is selected randomly as well within the defined segment (see FIG. 6). We chose a 1 nm fixed layer at the bottom of the cell to prevent the system motion during the consecutive irradiation.

We used periodic boundary conditions in the x-y directions and an open surface in the z direction. FIG. 6 illustrates how the irradiation process was carried out.

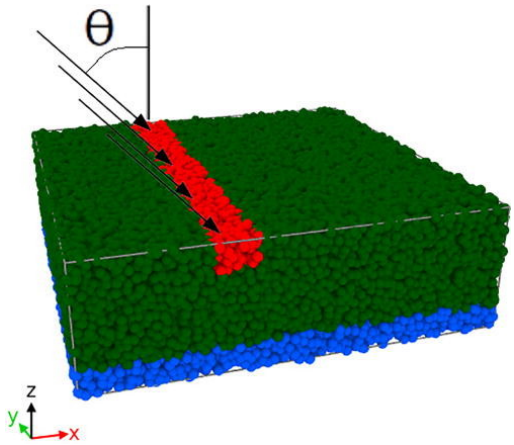

Figure 6: a-Si simulation cell. In red the irradiated segment. In blue the fixed region [Publication II].

The simulated time for every impact is 31 ps, divided in 21 ps applying a 0.8 nm thermal bath using the Berendsen thermostat [51], followed by 10 ps of cooling down to 300 K to prepare the cell for the next impact. Prior to the next impact, all the atoms which reached the fixed layer at the bottom are removed.

We simulated the following cases depending on the material used, ion energy and irradiation angle:

1. a-Si
   (a) 30 eV-Ar^+: 55°, 65°, 70°, 80°, 85°
   (b) 250 eV-Ar^+: 70°, 80°, 85°, 88°
   (c) 1000 eV-Ar^+: 70°, 80°, 85°, 88°

1. c-Al
   (a) 30 eV-Ar^+: 70°
   (b) 250 eV-Ar^+: 70°, 80°, 85°, 88°
   (c) 1000 eV-Ar^+: 70°, 80°, 85°, 88°

The analysis performed over the simulations helped us to understand which mechanism is more relevant in the "single-ripple" formation or the groove-ridge structure, differentiating between erosive and redistributive ones. The erosive mechanism occurs by the

sputtered atoms, i.e. the material which is removed from the system as a product of the incoming ions. The sputtering yield is defined as follows,

$$Y(N_{impacts}) = \left(\sum_{i=1}^{N_{impacts}} N_{sputtered} \right) / N_{impacts}, \tag{28}$$

where $N_{impacts}$ is the number of recoils used for the analysis and $N_{sputtered}$ is the atoms considered to be sputtered, in other words, those above a certain height over the surface after the irradiation. The redistributive mechanism is defined by the components of the total displacement vector,

$$\begin{aligned} \vec{\delta} &= \delta_x \vec{i} + \delta_y \vec{j} + \delta_z \vec{k} \\ \delta_u &= \sum_{i=1}^{N_{displaced}} (u_i^{final} - u_i^{initial}), \end{aligned} \tag{29}$$

where δ_u are the different components of the total displacement vector ($u = (x, y, z)$). These are defined as the total displacement in each direction from positions found in the initial structure. The total displacement is calculated based on these atoms which are displaced within the material, and accumulated displacement within the system can be evaluated in order to see its role in the eventual formation.

The analysis of both mechanisms allowed us to determine the cause of formation of surface structures. Besides, we can analyze the groove in terms of the volume generated in the material, considering the volume of the groove as follows:

$$V_{groove} = V_{orig} - V_{solid}, \tag{30}$$

where V_{orig} is the initial total volume of the cell and V_{solid} is the solid volume of the cell calculated using the surface mesh algorithm included in OVITO [67]. Alternatively, we can estimate the volume of the generated groove as follows,

$$V_{groove} = V_{sput} - V_{adatom} + V_{Ar} + V_{redist}, \tag{31}$$

where $V_{sput} = N_{sput} \cdot V_{atom}$ is the volume sputtered away, which is calculated as the number of sputtered atoms times the atomic volume, $V_{sput} = N_{adatom} \cdot V_{atom}$ is the total volume of atoms above the initial level of the surface, V_{Ar} is the accumulated Ar volume in the cell (which is neglected here since in all the cases it is lower than 1 %) and V_{redist} is the volume created by atomic redistribution in the cell. Hence, in case of ripple formation caused only by erosion, the volume of the groove would be $V_{no-redistribution} = V_{sput} - V_{adatom}$. The analysis is done using the atomic volumes for Si and Al which are 0.02 and 0.017 nm^3, respectively.

Therefore, collecting all this information, we are able to determine the cause of ripple formation either in a-Si or c-Al.

4.3.3 Accelerated MD

The methodolgy applied in [Publication **III**] is described in this subsection. The accelerated MD method was also applied for sequential irradiation, similar to that one described in Section 4.3.2, but there are substantial differences between them.

In several works [68, 69], it is stated that MD is not a suitable tool for studying the direct ripple formation due to time and size limitations, however, it is used to parametrize some established models. As some examples, we can see that the sequential irradiation methodology with MD has been successfully applied to study different effects such the stress accumulation [22, 25] or the relation of the stress due to ripple formation [23, 24]. In [Publication **III**], we prove that it is possible to obtain direct formation of a ripple in the sequential irradiation using MD. The aim is to speed-up the sequential irradiation process. The way to do that is to reduce the time span between the sequential impacts and after every ten simulations, recover the initial temperature of the cell. In order to do that, we have to measure correctly whether all the induced effects of the impacts are collected.

The simulations are divided in two types: the first starting from the flat surface (the cell used is the 73584-atoms-based one), in which we are using homogeneous irradiation over the whole surface choosing a random impact point. The second type is performed applying the same method, but in this case, the starting configuration is the resulting cell of 2000 consecutive impacts using the methodology explained in Section 4.3.2 containing 73353 atoms. In the first simulation, we aimed to create nanoripples in the surface and in the second, measure the velocity of propagation of an already-created structure at the same time as we see whether the ridge is playing a role in the formation of other structures on the surface [Publication **III**].

Fridlund et al. [28] introduced this *accelerated* method, which is explained as follows: every impact is simulated for 1 ps applying 0.8 nm-thick thermal bath at 300 K and, after every nine impacts, the system temperature is restored again to 300 K during 30 ps. The 1 ps long simulation time is enough to have a similar cumulative effect as was observed using longer simulation times, as was reported in [Publication **II**]. This kind of methodology allows us to reach higher fluences, and irradiating the whole surface, using less computational time. The fluctuations of the temperature during this procedure (reducing the time span between impacts) do not exceed 7 K with respect to the non-accelerated (relaxing after every impact (Section 4.3.2)) method, showing that both approaches do not differ much in the response to ion irradiation.

In this case, we also measure the total displacement vector and the number of sputtered atoms. Moreover, we measure the velocity of propagation in order to compare with experimental values as a function of the additional fluence [70]. The velocity is measured from the movement in the x direction (parallel to the ion beam projection) of a peak created in the cell.

There are no experimental results of the velocity of propagation at this low energy, but we can observe directly from the simulation how much the peak is displaced as a function

of the incoming fluence. Hence, using that information we can estimate the velocity.

5 BINARY COLLISIONS APPROXIMATION

The BCA is a simulation method of quite extended use and very efficient for the study of energy cascades [54, 71]. The transmitted energy (EQ. 21) and the scattering angle are used to calculate the interaction between the incident atom and the atoms in the subtract. In order to simulate the process, a description of the parameters involved in the calculation is needed. The atomic density of the target is included, which will contribute to the probability of finding an atom by the incident atom, since it is related to the impact parameter is randomly selected within the scattering cross-section. Other parameter is the cut-off energy, which determines that only particles above certain value will be considered; and the threshold displacement energy, which marks the value needed to displace an atom from its initial position. The modification of these parameters are crucial for the correct reproduction of the cascades, and, indeed, will determine the how fast the simulations run.

In [Publication **I**] we used a parametrization developed by Bukonte et al. [65], which was tuned for a-Si. The simulations were performed using the CASWIN code [72].

6 EXPERIMENTAL EVINDENCE OF RIPPLES FORMATION

In this section we discuss briefly the different experimental methods used to generate and analyze the ion-induced nanopatterning on surfaces.

6.1 Ion irradiation

In general, different structures can be generated by using prolonged tilted ion-beam irradiation: from quantum dots to oriented ripples [5] modifying the conditions of the experiments. The role of the ion energy or the irradiation angle are thoroughly discussed in this work (Section 1), however, other factors have an extended influence on the surface modification. Variables such as pressure, temperature, rotation of the sample, substrate or fluence have a major role in the generation of nanostructures. The tuning of those parameters will be determinant in order to observe the expected result.

In this subsection, we summarize and give examples of the importance of such experimental conditions.

The irradiation of the samples is done using high [Publication **II**] [73] to ultra-high vacuum chambers [10, 40, 74–76]. These conditions are needed in order to perform surface analysis and thin film growth as well.

The substrate temperature can oscillate from low to high temperature. At low temperatures, such as 80 and 130 K, we can find the irradiation of Si surfaces using 4.5 keV-He [77], where the diffusion will play a role different from that at higher temperatures. Usually the nanopatterning effect has been studied under room temperature conditions [10, 78], obtaining various types of structure formation. Reference [79] reports that in Si over 643 K the created vacancies annihilate with the adatoms, so no adatom island formation is observed. Also in the range of temperatures between 213 and 333 K [80] the ripple production was studied. Island-like structures were observed at higher temperatures 973 K. Also at higher energies, between 873 and 1473 K, craters were induced in Si [81].

Depending on the energy and the material of study, the onset of the rippling effect varies with fluence. For instance, the fluence needed to observe ripple formation in Si is in the order of 10^{17} ions/cm^2, while for a metal the fluence is about 10^{15} ions/cm^2 [82]. The fluence is directly related to the irradiation time, and it can play an important role in the orientation of the ripples. For example in [83] we can see how the exposure to Ar^+ irradiation makes the amplitude and the wavelength change on Si(100) as a function of flux, leading to two different regimes from linear to non-linear .

The sample is normally fixed to a base in order to produce nanoripples, so the fluence is accumulated in a specific direction and not homogeneously. Rotation of the sample can produce different structures such as hexagonal arrays of Si-nanodots [75]. In [84], we can observe how the rotation of the sample every certain time span, alongside with the

accumulation of fluence, can create ripples oriented parallel and perpendicular to the ion beam projection.

6.2 Scanning electron microscopy

The scanning electron microscopy (SEM) [85] is a type of microscopy of extended use in the materials field, since it has some advantages over the conventional transmission or reflection electron microscopies [86]. The electrons from the source interact with the sample which is being analyzed, and produce several signals that are processed in order to determine the surface topography and composition [87]. The imaging process starts with the generation of a beam of energetic electrons which travels toward the sample, being focused by different magnetic lenses [88]. These electrons carry a known amount of kinetic energy which is deposited in the sample, and due to the interaction, other electrons are scattered and collected, and the scatter patterns provide information on shape and composition of the sample. Nevertheless, the amplitude of the nanopattern cannot be measured directly because SEM does not account for the depth in the sample [89], however it can be done with other techniques such as the atomic force microscopy (AFM).

This technique is quite well-spread in the nanopatterning characterization and used in several studies [70, 90, 91], allowing to determine the shape of the surface after the ion beam effect over the material and its evolution. In cases of high roughness, the penetration of the electrons plays an important role in determining the observation of details, at a considerable depth within the material.

6.3 Atomic force microscopy

The atomic force microscopy (AFM) was introduced in 1986 [92] as a new method for materials analysis. The interatomic and electromagnetic forces are the driving force to use AFM. It consists of a tip which can move along the surface. The tip-sample interaction [93] provides the information of the measurement, i.e. the force between the tip and sample due to the tip-sample interaction potential (V_{ts}) in the z direction,

$$F_{ts} = -\frac{\partial V_{ts}}{\partial z}. \tag{32}$$

This force will provide the information needed to profile the surface measured by the cantilever [94].

In AFM there are three different operation modes [93, 95]: contact mode, non-contact mode and *tapping* mode. In the contact mode, the tip moves through the sample in close contact with the surface. The non-contact mode is based on the attractive Van der Waals forces between the tip and the sample. In this case, the response is weaker than in the contact mode, but it is used in cases where the tip cannot be in contact with the sample

because of possible introduction of changes in the sample. The tapping mode provides a high-resolution topographic picture of the surface which can be altered. This mode consists of the oscillation of the tip over the surface, avoiding the destructive frictional forces that can occur in the contact mode in case of fragile samples.

This technique is commonly used in order to characterize the sample during the irradiation process. The microscope allows to measure, besides the wavelength, the amplitude of the patterns. This height consideration is something that cannot be observed using other techniques [Publication **II**] (see FIG. 7), so using AFM we can determine at how deep the surface was affected by the irradiation, or the amplitude of the periodic structures formed over the surface.

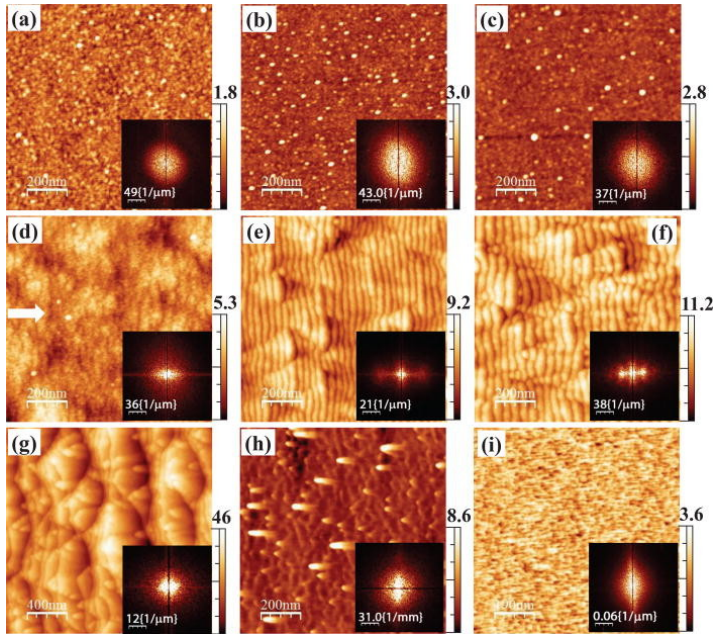

Figure 7: AFM images of the evolution of the Si surface under 30 eV-Ar^+ irradiation at ion incidence angles: (a) 0°, (b) 25°, (c) 35°, (d) 55°, (e) 65°, (f) 70°, (g) 75°, (h) 80° and (i) 85°. The inset shows the corresponding FFT images and the white arrow points in the direction of the incoming ions. [Publication II].

7 CRATER FUNCTION RESULTS

The outcomes of the application of the model explained in Section 4.3.1 and 3.2 are shown here. The results included in [Publication **I**] and [Publication **II**] are presented in this section, giving special attention to the results derived from from the crater function formalism [19].

The coefficients governing the stability of the surface (eq. 11) are presented here for 30 eV-Ar^+ on a-Si.

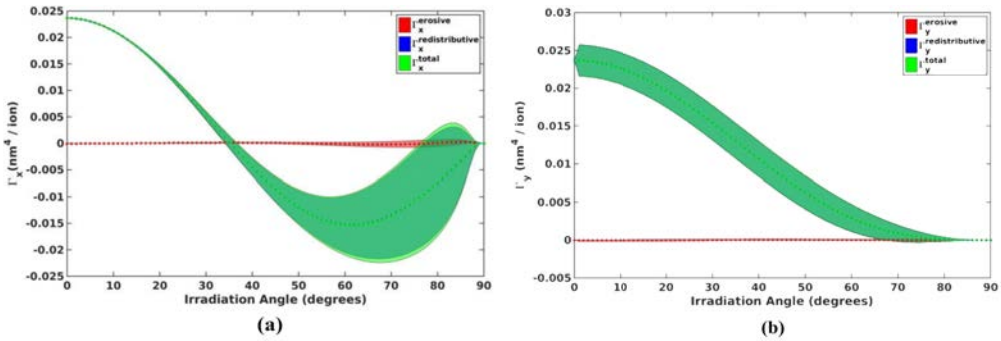

Figure 8: Results for single 30 eV Ar^+ on a-Si. (a) Γ_x (b) Γ_y. The shaded regions represent one σ confidence interval and the dotted lines the mean. From [Publication II].

As we can see in the FIG. 8, the erosive contribution (red area) to the total (green area) is minimal, the total coefficient ($\Gamma_{x,y}(\theta)$) is entirely governed by redistribution (blue area) since the sputtering is almost not contributing to the pattern formation, as shown in the experiments and sequential simulations shown in Section 8.1. At this low energy, the contribution of the erosion to the pattern formation can be almost neglected.

In FIG. 9 we compare the results obtained using MD and BCA for 1000 eV-Ar^+ on a-Si. Since both methods have principle differences in the algorithm regarding the interactions between the atoms involved in the process, it is interesting to analyze the effect of the differences. First, the unstable region (below zero) starts at lower angles for MD than for BCA. The redistributive coefficient is greater in case of MD, since the total displacement measured in the MD simulations is greater as the small displacements cannot be captured by BCA [Publication **I**]. In both methods, the erosive coefficient becomes more positive at around 75°, which acts as a stabilizer of the total coefficient in the x direction (FIG. 9 a, c). On the other hand, in the BCA, the erosive effect is the principal contributor to the stability of the surface, and again acts as provider of stability at grazing incidence (FIG. 9 c). In both cases, the increase of the erosive contribution occurs at around the same angle. Moreover, for both MD and BCA, we observe a domination of the Γ_x over Γ_y indicating the instability of the surface. The importance of this result will be discussed later for the prediction of the pattern wavelength.

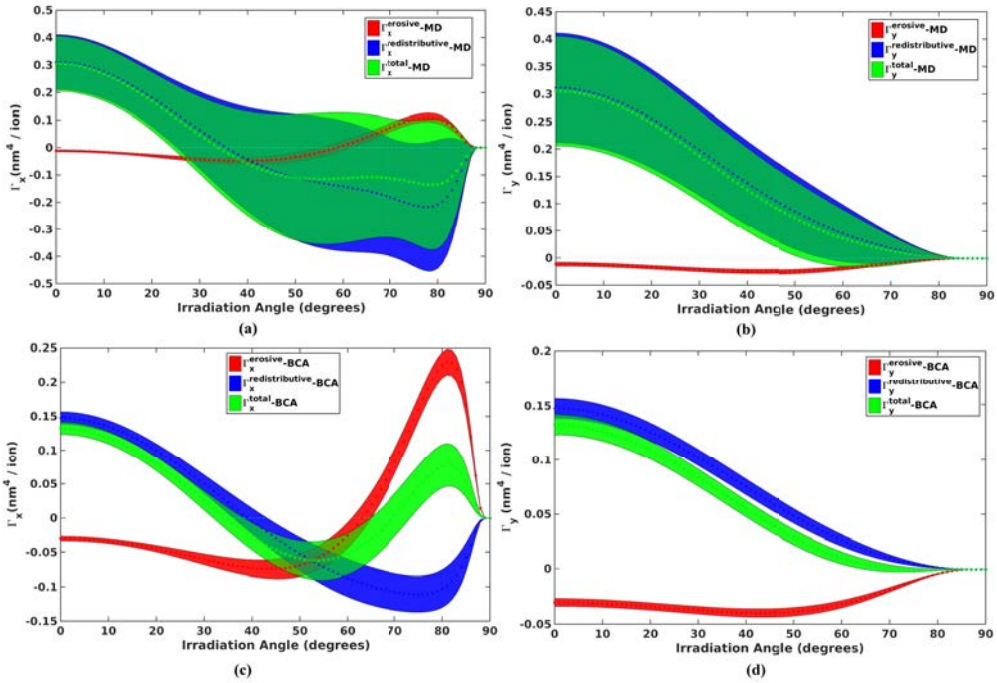

Figure 9: Results for single 1000 eV Ar^+ on a-Si. For MD (a) Γ_x and (b) Γ_y, and for BCA (c) Γ_x and (d) Γ_y. The shaded regions represent one σ confidence interval and the dotted lines the mean. From [Publication I].

Using the coefficients calculated in FIGs. 8 and 9, a prediction of the wavelength is done using eq. 27. In this case the angle dependent $B(\theta)$ is used for the 30 eV results. The prediction of the wavelength for ripple formation for 30 eV is as shown in FIG. 10,

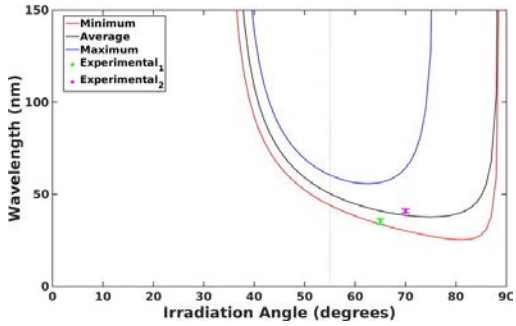

Figure 10: Wavelength prediction for single 30 eV Ar^+ on a-Si (using a flux of 3.25×10^{14} cm^{-2} s^{-1}). The predictions are done using the values of lower and upper bounds and mean from FIG. 8. Experimental$_1$ = 35.3±1.5 nm (parallel) and Experimental$_2$ = 40.9±1.1 nm (parallel) (from experiments shown in FIG. 7). The magenta dashed line represents the critical angle. From [Publication II].

In FIG. 10, we can see how the prediction of the wavelength is in considerably good agreement with the experiments. We observe that the 65° is within the limits of the prediction and the 70° is almost coincident with the average value of the prediction. This good agreement comes from the redistributive contribution. This contribution gathers the small displacements (decisive, specially in this case, due to low irradiation energy) which make the final prediction quite accurate, in addition to the angle-dependent B(θ) coefficient.

At 1000 eV, the prediction was implemented with MD and BCA, using a constant value for the viscous flow coefficient (B(θ) = 0.062 $nm^2 s^{-1}$), which worked reasonably well. The prediction is shown in FIG. 11. As we can see in the figure, both predictions are different. The MD prediction is closer to the experimental value provided by Madi et al. [41] than the BCA prediction, but the latter is closer in its prediction of the critical angle, i.e. the prediction starts at 31° (25° in the case of MD). We can see that for these energies, the contribution of the redistribution (see FIG. 9 a) plays more important role in surface formation, that is the reason for a better estimation of the wavelength in MD than in BCA, where the erosion is having a greater role on the instability of the surface (see FIG. 9 c). On the other hand, using MD, the perpendicular wavelength is not predicted , because the contribution of the $\Gamma_y(\theta)$ does not reach the unstable regime in comparison with$\Gamma_x(\theta)$, while using BCA it is. Moreover, there no upper limit for the prediction (FIG. 11 a), because the upper bound corresponding to the coefficient in FIG. 11 a is over zero (stable regime) for the whole range of angles .

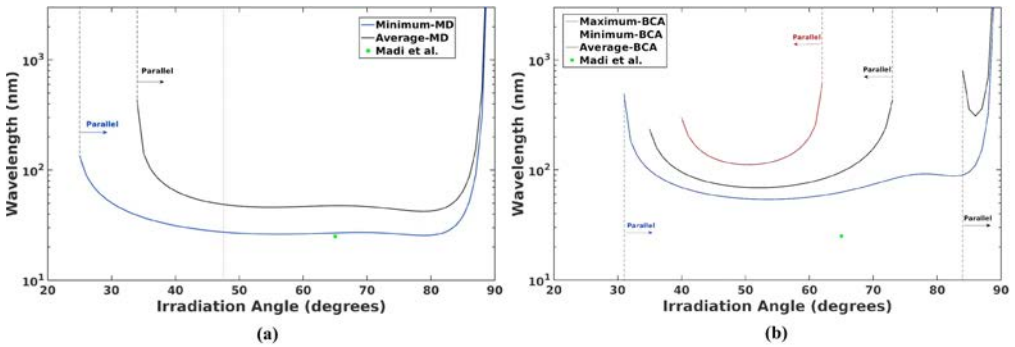

Figure 11: Wavelength prediction for single 1000 eV Ar^+ on a-Si (using a flux of 2×10^{12} cm^{-2} s^{-1}) for (a) MD and (b) BCA. The predictions are done using the values of lower and upper bounds and mean from FIG. 9. The green point is 25.0 nm (parallel) (from experiments measured in [41]). The magenta dashed line represent the critical angle. From [Publication I].

8 DIRECT SIMULATION OF RIPPLE FORMATION

In this section we discuss the main results based on the segment irradiation simulations (Publication II and IV) at low and medium energy performed over a-Si and c-Al. We compare the simulations performed with experiments and the different effects of the irradiation over an amorphizable surface of a semiconductor (Si) and non-amorphizable surface of a metal (Al).

8.1 30 eV simulations vs experiments

In this subsection, we include the simulations performed with ultra-low energy (30 eV) using the methodology explained in Section 4.3.2. This model of simulation was intended to reproduce a significant deformation of the surface in a relatively short time span. The motivation of studying the surface modification at such low energy is recent experimental observation of ripple formation at this energy as well. Experiments on Si at 30 eV were included in [Publication **II**], alongside the proposed model to study the mechanisms of formation of these ripples. The cross-section of final configuration as a result of simulation of linearly focused ion irradiation on a-Si can be observed in FIG. 12,

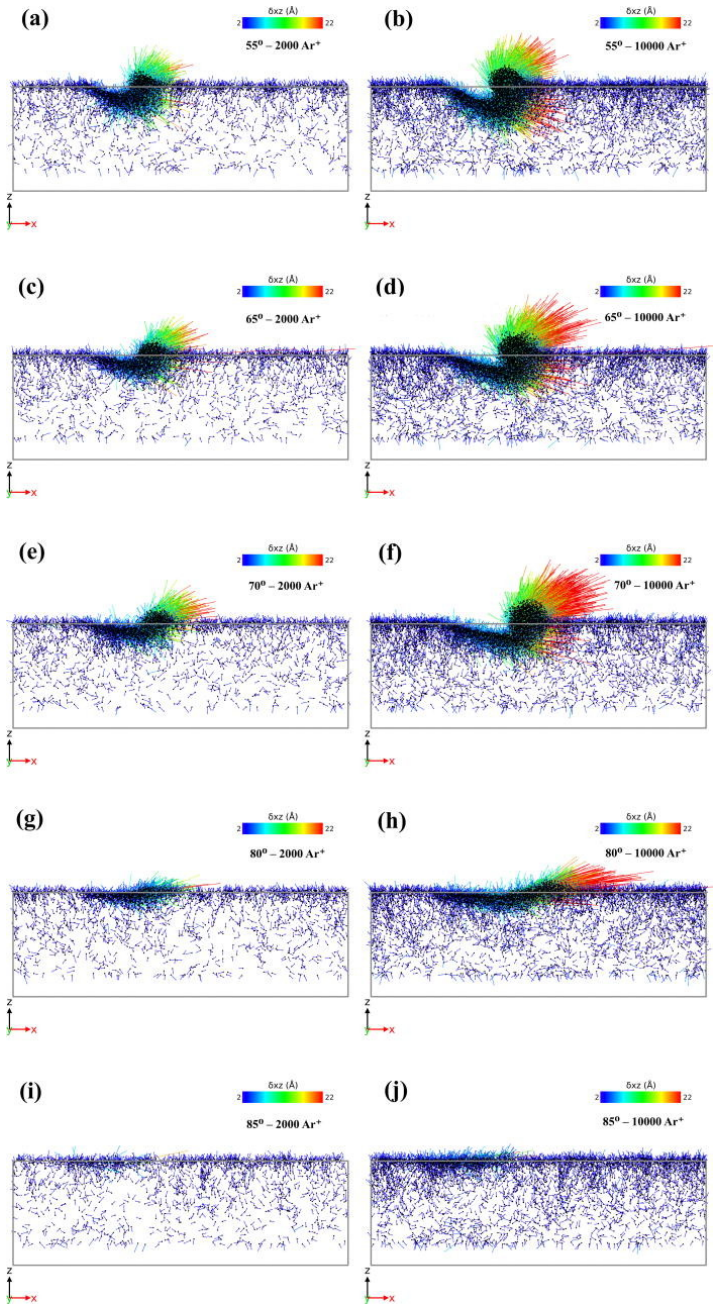

Figure 12: a-Si cell under 30 eV Ar^+ at 55° ((a) and (b)), 65° ((c) and (d)),70° ((e) and (f)), 80° ((g) and (h)) and 85° ((i) and (j)) after 2000 and 10000 impacts, respectively. The displacement vectors are coloured according to their magnitude and shifted for clarity. From [Publication II].

In these images we can see how the displacements are accumulated in the sample as a function of the incoming ions and, accordingly, the groove is increasing in its size as well, however, differently for the different angles. We can see that in the cases of 65° (FIG. 12 d) and 70° (FIG. 12 f) the effect is clearer than in the other cases. For the angles closer to grazing incidence, the effect is much less noticeable. Eventually (FIG. 12 j) the only displacements we can observe are those performed by surface atoms. The accumulated number of sputtered atoms and accumulated displacement during the performed simulations (FIG. 12) are plotted in FIG. 13,

In FIG. 13 a, the maximal sputtering efficiency is observed in the 80° case, with the number of sputtered atoms continuously growing until the end of the simulation. We can see as well that in the first thousands impacts at 70° the sputtering is higher than for 80°, however, eventually the sputtering at 70° is the second highest, because the slope of the growing starts to decrease gradually and, at some point, it stops increasing and reaches a saturation, as in the cases of 55° and 65° at different points of the irradiations process. The change in the induced displacement and the surface morphology drive the sputtering yield to change. In the case of 85°, only 3 atoms are sputtered.

FIG. 13 b shows similar results for displacement accumulation in the $x - z$ direction for 55°, 65° and 70°, but for the latter, the accumulation of displacement is somewhat higher. For 80° and 85° it is considerably lower, with 80° being the highest among these two. We can see that the surface modification is highly related to the induced displacement in the sample (see evolution in FIG. 12). In FIG. 13 c, we can observe separately the two components, x and z, because y oscillates around zero during the whole simulation; the x component is lower in all the cases than the z, so the z component dominates the value of the total displacement, and is mainly affected by the open surface in the z direction. The x component is higher in those cases where the ridge on the surface is more obvious (55°, 65° and 70°), and in the case of 80° the induced displacement is lower than in the other cases, leading to a less apparent ridge over the surface (see FIG. 12 h). For 85°, the induced displacement fluctuates around zero, showing that the effect at the surface is almost negligible.

The analysis performed in this work showed us that, in the highest case (80°), the total number of sputtered atoms is 110, giving a sputtering yield of 0.011, which is really low. The experiments performed in [Publication **II**] provided information about the pattern formation at such low energy, and our analysis reveals that the displacement is the reason of such formation. That is, even, under an almost-complete absence of sputtering, the formation of ripples is possible.

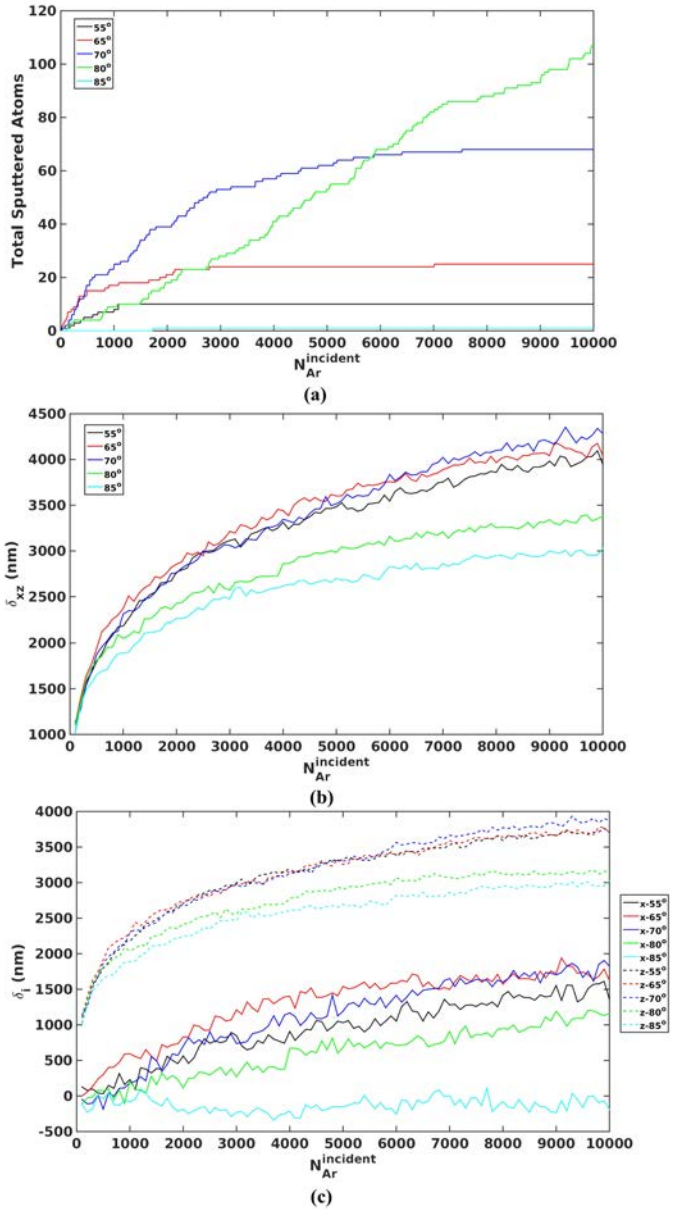

Figure 13: Results for total sputtering (a), total displacement in the x-z direction (b) and individual components of the total displacement (c). From [Publication II].

8.2 Comparison of a-Si and c-Al

In this subsection, we discuss the results obtained for a-Si and c-Al, comparing both of them [Publication **IV**] and setting up conclusions about the pattern formation on both materials, having clear differences between them. The cells used for this study are

described in Section 4.2.2 for a-Si and Section 4.2.3 for c-Al. The evolution of sputtering and displacement vector will determine the eventual formation of any structure over the surface, and this analysis is given here. In addition, we provide a volume analysis in order to see the reasons of groove formation, as was explained in Section 4.3.2.

We have simulated up to 10000 Ar impacts for 30 (only for 70° off-normal) and 250 eV. In the case of 1000 eV Ar^+ irradiation, the results are limited to 4000 impacts. The reason of this is that the energy is sufficiently high to provoke enough erosion at larger fluences that the cell cannot hold because of size requirements. In the case of a-Si, the effect is shown in FIG. 14 for 250 and 1000 eV.

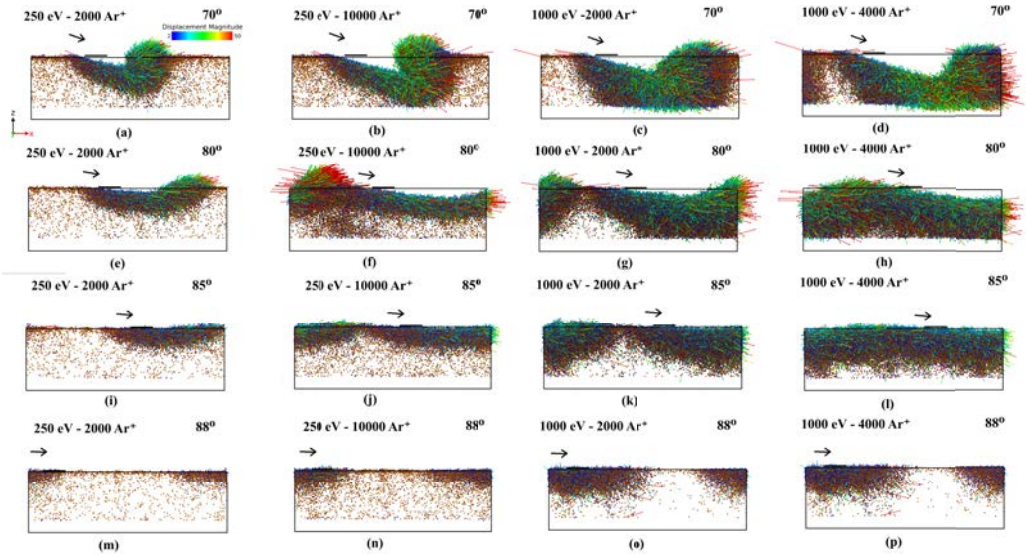

Figure 14: a-Si cell under 250 eV Ar^+ at 70° ((a) and (b)), 80° ((e) and (f)), 85° ((i) and (j)) and 88° ((m) and (n)) after 2000 and 10000 impacts, respectively, as well as a-Si cell under 1000 eV Ar^+ at 70° ((c) and (d)), 80° ((g) and (h)), 85° ((k) and (l)) and 88° ((o) and (p)) after 2000 and 4000 impacts, respectively. From [Publication IV].

In FIG. 14 we can see how the surface changes differently as a function of the energy and irradiation angle. In the case of 250 eV irradiation, we observe how the most abrupt effect in the surface profile takes place at 70° (FIG. 14 a and b), while the impact region is changing as the ions induce displacement and create a ridge growing upwards. In the 80° (FIG. 14 e and f) case, we see how the effect is less noticeable than in the 70°, but the accumulation of displacement in the x-direction is still clear, forming a smaller ridge. For 85° (FIG. 14 i and j) only at the end of the simulation we can observe a small effect in the surface profile; and for 88° (FIG. 14 m and n) the effect of the ions on the surface is almost negligible.

Regarding the 1000 eV results, we see that for 70° (FIG. 14 c and d) the effect is again the clearest, but in this case differs from the 250 eV-70° case, because no ridge is formed

but a big momentum is induced in the x-z direction, creating a big groove. In the case of 80° (FIG. 14 g and h), we observe a similar effect, as the one for 250 eV, but stronger. For the 85° (FIG. 14 k and l), the same situation takes place: a greater change in the surface morphology is observed at 1000 eV compared to that created by 250 eV, an appreciable increase of the displacement and a more significant groove is created. In the case of 88° (FIG. 14 o and p), the effect goes in the same direction as the one for 250 eV, however, with the higher irradiation energy, the displacement in the surface is larger. In general, we conclude that, as one can expect, the erosion in these cases is considerably high and may play a significant role in pattern formation.

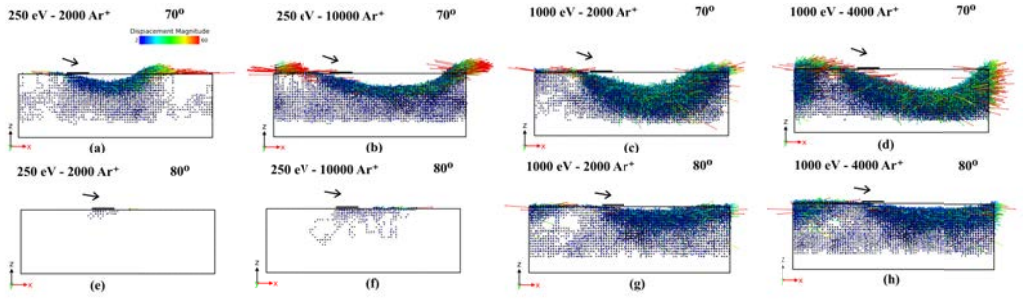

Figure 15: c-Al cell under 250 eV Ar^+ at 70° ((a) and (b)) and 80° ((e) and (f)) after 2000 and 10000 impacts, respectively. And c-Al cell under 1000 eV Ar^+ at 70° ((c) and (d)), 80° ((g) and (h)) after 2000 and 4000 impacts, respectively. From [Publication IV].

Now, we focus our attention on the c-Al case. In FIG. 15, the evolutions of the 85° and 88° are not included, because for these angles, there is no clear action over the surface induced by the incoming irradiation at any of the energies. For 250 eV in the 70° case (FIG. 15 a and b), we observe the largest change for this energy, inducing a groove and accumulating some atoms above the surface, building-up a ridge. In the case of 80° (FIG. 15 e and f), we observe that the effect is quite small compared with the 70° irradiation. Moving to the 1000 eV, the situation is different because we see that the modification is deeper in both cases. For 70° (FIG. 15 c and d), we observe a similar effect as for 250 eV at the same angle, but much more pronounced and for less fluence. The irradiation creates a larger groove in the material. In the case of 80° (FIG. 15 g and h), we observe that indeed the change is higher than for the lower energy, creating a small ridge-groove structure that was not observed in the 250 eV case. In general, less accumulated displacement is observed than in the case of a-Si.

The data regarding the redistributive and erosive effects are shown in FIG. 16. As we can see in FIG. 16, the effects are different in each material. We can see how the induced displacement in both directions (x and z) is higher in a-Si than in c-Al (compare FIGS. 16 c and 16 d, and FIGS. 16 e and 16 f). The reason of this difference is because of the small displacements that are induced in the amorphous material and are absent in the crystalline one (see FIG. 17), and their contribution is considerable. On the other hand,

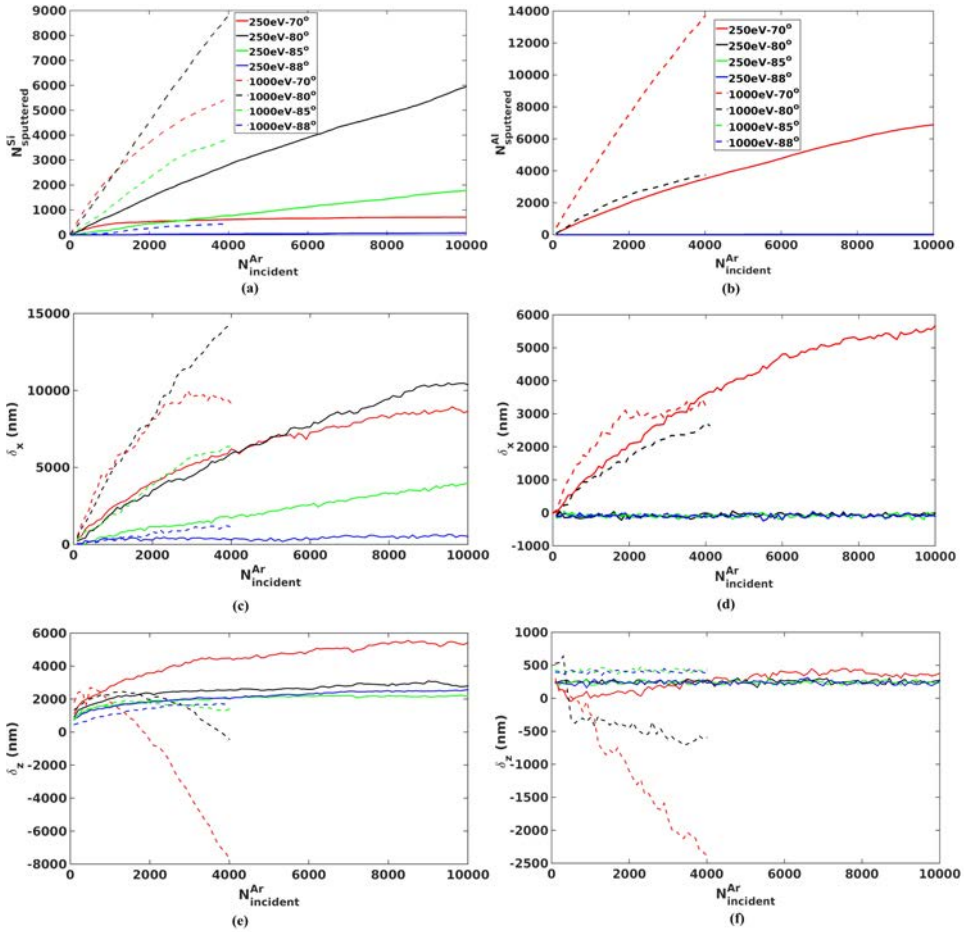

Figure 16: Results for total sputtering, (a) and (b), total displacement in x-direction, (c) and (d), and total displacement z-direction, (e) and (f), for a-Si and c-Al, respectively for 70°, 80°, 85° and 88°. From [Publication IV].

the erosion is higher in the case of the crystalline material. In the case of Si, FIG. 16 a shows how the sputtering affects the change of the surface morphology at 70° (seen in FIG. 14 a and b). This effect makes the sputtering yield smaller than in the case 80° at the end of the simulation for 70°. On the other hand, the sputtering is greater for 70° in the first stages of the simulation, but as a consequence of the induced change in surface morphology, the incidence angle is modified and, consequently, the evolution of the sputtering yield. This effect occurs in both 250 and 1000 eV simulations. The results at 85° and 88° are considerably lower. For 250 eV, the erosion for 88° is almost negligible. In the case of 88° at 1000 eV, the effect is higher. In the case of the induced displacement in the x-direction (FIG. 16 c) we observe a similar trend for 70° and 80°. The displacement is higher in the case of 70° at the beginning of the simulation, but at some point (about 5000 impacts for 250 eV and 2000 impacts for 1000 eV) the accumulation of displacement

in the 80° is greater for 250 and 1000 eV. In the latter case that happens sooner due to a more noticeable change of the surface morphology (see FIGs. 14 a and 14 c, and FIGs. 14 e and 14 g, respectively for 250 eV and 1000 eV). The accumulation of displacement at 85° and 88° is lower than in the rest of cases, but the effect is higher at 85° than at 88°, and indeed higher for 1000 eV than for 250 eV. FIG. 16 e shows the evolution of the accumulation of displacement in the z-direction. We observe that a growth of the accumulated displacement is stronger for 250 eV energy at 70° than the remaining cases of different angles, with the resulting structure as shown in FIG. 14 b. The change of the sign in growth of δ_z in the case of 70° and 80° at 1000 eV (see FIGS. 16 e and 16 f) is due to preferential displacement of atoms (which are not sputtered away) inwards the surface in the negative direction, due to strong transfer of momentum in this direction.

In the case of Al, we can observe that even at 1000 eV no damage is created in the surface at 85° and 88°, so only for 70° and 80° we can observe any noticeable effect. In FIG. 16 b, we see how the sputtering increases in the case of 70° and 80°. For 250 eV, we only see a clear effect for 70°, not for 80° due to low deposition of energy in the material at that inclination. At 1000 eV, we observe erosion for both cases, but considerably higher in the case of 70°. In FIG. 16 d, we see how the accumulated displacements in the x-direction grow faster for 70° than for 80° at 1000 eV, but in the case of 70° at 250 we see that at 4000 impacts, the accumulated displacement is larger than in the case of 1000 eV. The reason for this result is that the erosion is modifying the surface morphology and, consequently, the erosion plays more important role in surface modification at higher energy than the accumulation of displacement. In FIG. 16 e, as in Si, we observe how at the beginning displacements are accumulated positively, but at some point this trend changes and becomes negative, showing that the incoming ions are pushing the material inwards the surface.

A deeper analysis is performed at 70° for all the energies, including also results at 30 eV (for Si from [Publication **II**]). Doing that study we can measure the different contributions to the surface modification, i.e. redistribution, sputtering and adatoms, as a function of the energy used and the response of both materials. The comparison between them can be seen in FIG. 17, where the histograms are built as functions of the magnitude of the induced displacement per atom ($r = \sqrt{\delta_x^2 + \delta_y^2 + \delta_z^2}$).

FIG. 17 shows that the distribution of the induced displacements in both materials are quite different. In the case of a-Si we can see that most of the displacements induced are small (below 0.25 nm). The highest number of small displacements takes place at 30 eV, and it starts to decrease as the ion energy increases, providing higher displacements at 250 and 1000 eV, as can be seen in the tail of the lines in FIG. 17. On the other hand, in the c-Al case, they are clearly almost discretely located at the different nearest neighbour (NN) distances. There is no induced displacement at 30 eV since the energy is not high enough to displace any atom. However, we can see that it is at the 1NN distance where the atoms are trapped the easiest, while the 2NN is the second distance most common in the 250 eV case and 3NN is the second at 1000 eV.

We can analyze for 70° the evolution of the volume created in both materials at different

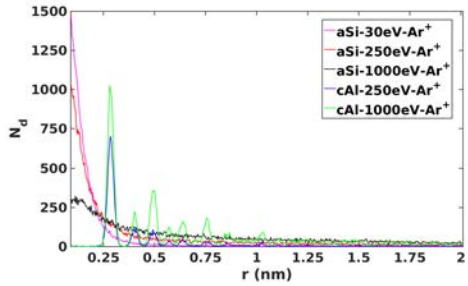

Figure 17: Number of displacements as a function of the magnitude of those displacements after 4000 Ar^+ impacts at 70°. Displacements below 0.1 nm are omitted (no appreciable displacement for 30 eV Ar^+ on c-Al). Data regarding 30 eV Ar^+ on a-Si is adapted from [Publication II]. From [Publication IV].

energies (described in Section 4.3.2) and also the displacement induced in the x-direction in order to determine the difference between the erosive and redistributive effects.

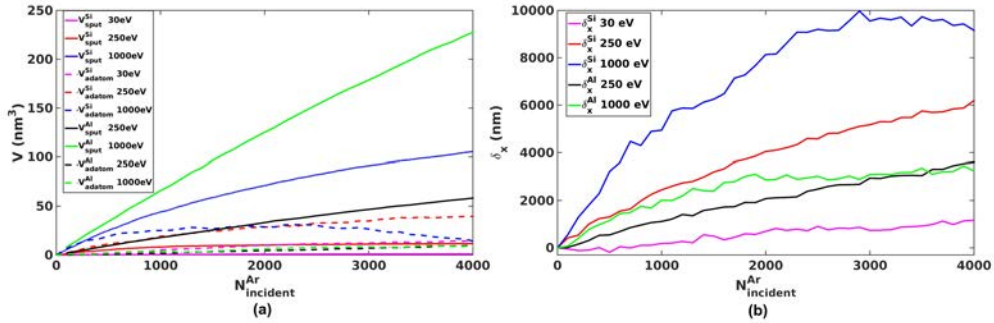

Figure 18: Evolution of (a) the volume created by the sputtered atoms and adatoms and (b) the accumulated displacement in the x-direction for 30 eV, 250 eV and 1000 eV Ar^+ for a-Si and for 250 and 1000 eV Ar^+ for c-Al at 70°. Data regarding 30 eV Ar^+ on a-Si is adapted from [Publication II]. From [Publication IV]

In FIG. 18 a, we can see how the volume sputtered (V_{sput}) is considerably higher since the beginning of the simulation for c-Al than for a-Si, except for the case of 30 eV. This energy is not enough to create any defect in the c-Al surface. The V_{adatom} in general is higher in the case of a-Si. The total displacement in the x-direction is also higher for Si. In general, the induced displacement is higher as the energy increases, and as we can see also in FIG. 16, the induced displacement is higher in a-Si than in c-Al.

Now we can quantify how the created ridges are formed as a function of the energy and the material involved after 4000 Ar^+ impacts.

As we can see in TABLE 1, not only the volume of the groove is different in each case, but the contributing factors for the formation of those grooves are not the same for the

Table 1: Volume loss induced by irradiation in a-Si and c-Al targets after 4000 Ar^+ impacts at 30 eV [Publication II], 250 eV and 1000 eV. The units are nm^3. From [Publication IV]

	V_{groove}	$V_{no-redistribution}$	V_{sput}	V_{adatom}
30 eV Ar^+ - a-Si	54.93	-13.74	1.09	14.83
250 eV Ar^+ - a-Si	67.21	-27.82	11.76	39.58
1000 eV Ar^+ - a-Si	241.3	91.17	105.56	14.39
250 eV Ar^+ - c-Al	113.58	48.49	58.27	9.78
1000 eV Ar^+ - c-Al	281.12	218.44	227.58	9.14

two materials. For a-Si, we can see that only in the case of 1000 eV, the $V_{no-redistribution}$ reaches 38 % of the V_{groove}, revealing that the redistributive mechanism is the driving force of the surface modification (about 62 %). We can see as well that for example in the case of 30 eV in a-Si, the groove is almost fully formed by redistribution [Publication **II**]. On the other hand, for c-Al the results are quite different: we can see that for 250 eV, the $V_{no-redistribution}$ is taking a more predominant role than in a-Si, reaching 43 % (considering only V_{sput} about 50 %) and is considerably higher at 1000 eV, constituting 78 % of the total volume of the groove.

In the light of these results, we can state that erosion is the main mechanism of the pattern formation in crystalline materials such c-Al, however, on the other hand, the redistribution is the most likely mechanism for the pattern formation in a-Si. At higher energy the role of erosion becomes more important, but is not higher than the redistribution contribution, even at 1000 eV irradiation.

This "single-ripple" formation model presented here provides a good insight towards understanding of the reasons for the ripple creation on surfaces, analyzing the volume of the groove, via the sputtering and adatoms, and the accumulated displacement.

8.3 Direct observation of ripple formation during homogeneus irradiation

In this section we discuss the results shown in [Publication **III**]. Here, using an accelerated method [28], we can simulate the direct atomic reorganization in the surface, and besides, predict a velocity of propagation in reasonable agreement with the one measured experimentally [70]. Using the methodology and structures detailed in Section 4.3.3, we proceed to present the simulation results.

In FIG. 19 we show the evolution of the initially flat surface under irradiation.

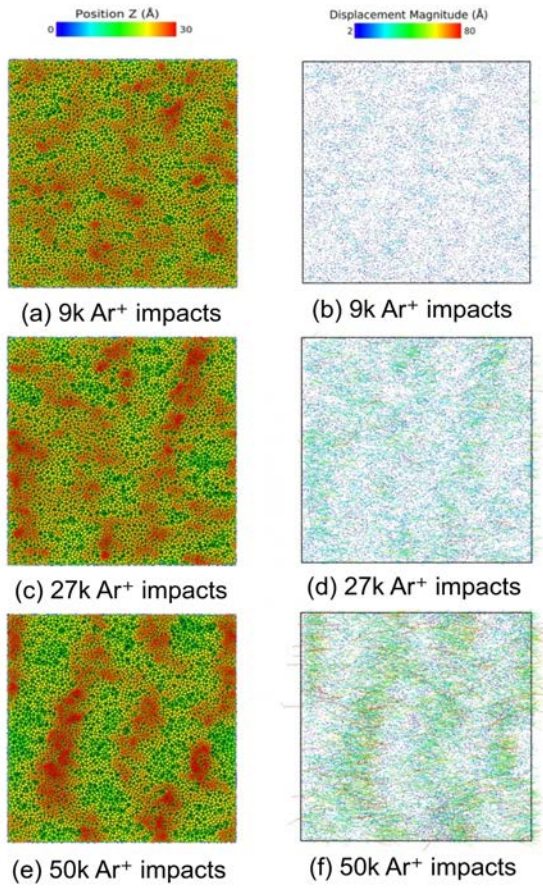

Figure 19: Evolution of the initially flat surface under random impact 30 eV-Ar^+ at $\theta = 70°$. In (a), (c) and (e) we see the height of the surface and in (b), (d) and (f) we plot the displacement vectors greater than 2 Å (located at the final position and shortened by a factor of 1/5 for a better observation) from the initial configuration. From [Publication III].

In FIG. 19, we see the evolution of the surface at 9000, 27000 and 50000 impacts. It is noticed how the effect of the incoming ions becomes more apparent due to the reorganization of the atoms in the surface. The evolution of the height in the surface can be followed in FIG. 19 a, c and e, where it is noticed that ripples are formed as the fluence increases. In FIG. 19 b, d and f we see how the displacement is accumulated, mostly in the x-direction. At first, a random roughening is created. After about 20000 impacts, we can observe how these crest-trough structures become more apparent. Once the ripples are formed, they start to propagate on the surface.

In order to understand the nature of driving forces, we simulated the evolution of a not-flat initial surface. This case was created to see how a single ridge in the surface influences the evolution of the surface. The results are shown in FIG. 20.

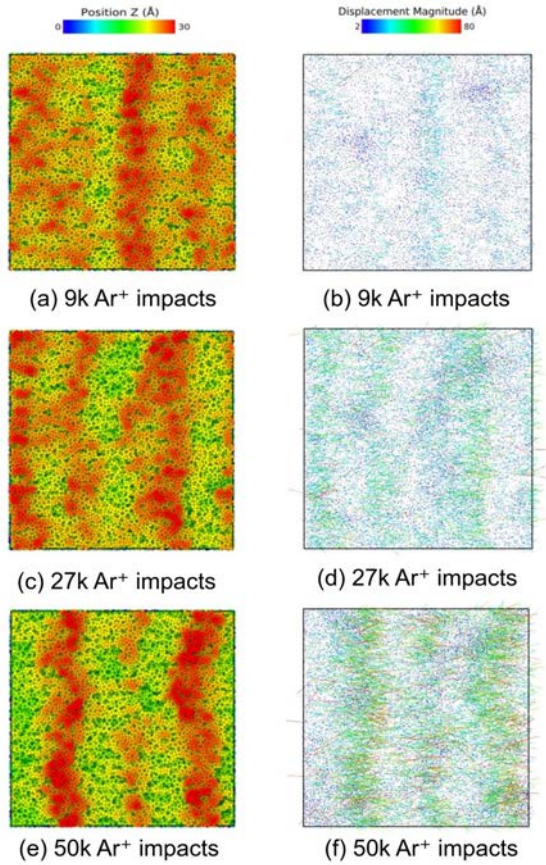

Figure 20: Evolution of the initially not-flat surface under random impact 30 eV-Ar^+ at θ = 70°. In (a), (c) and (e) we see the height of the surface and in (b), (d) and (f) we plot the displacement vectors greater than 2 Å (located at the final position and shortened by a factor of 1/5 for a better observation) from the initial configuration. From [Publication III].

We observe how the effect of the ridge plays a role in the way that the creation of more structures in the surface occurs on the initially-flat surface.

We can extract data regarding the displacement and erosion from the cases presented in FIGs. 19 and 20.

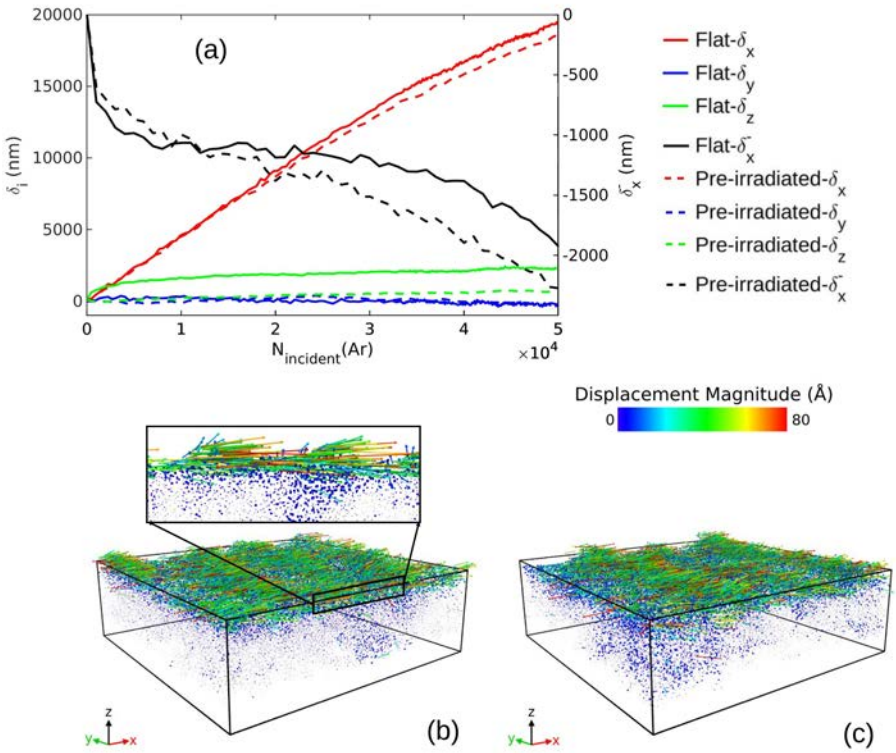

Figure 21: (a) Evolution of the different components of the displacement vectors δ (on the left vertical axis) and only negative contribution in the x-direction δ_x^- (on the right vertical axis) as a function of the number of incoming ions from the initially flat surface and the surface with a pre-existing ridge. (b), (c) Displacement vectors (located at the final position and shortened by a factor of 1/5 for clearer observation) from the initial configuration in the initially flat (b) and pre-existing ridge (c) surfaces. The black rectangle represents a closer view of the displacement vectors (shortened by a factor of 1/2) in one of the ridge areas (a 1.5 nm-thickness slice in the y-direction). From [Publication III].

In FIG. 21 a, we can see the three components of the total induced displacement for the flat and the pre-irradiated surfaces, as described in eq. 29. We represent the evolution of δ_x, δ_y and δ_z. The y-component fluctuates around zero due to symmetry considerations. In both simulated cases, there is a linear increase of the number of sputtered atoms with fluence. The average sputtering yield are $S_y = 0.03$ for the initially flat surface and a slightly higher value ($S_y \approx 0.04$) for the pre-irradiated surface. Nevertheless, comparing

these values to the one obtained in [Publication **II**] for the single impact calculations ($S_y = 0.035 \pm 0.013$), the calculated values are somewhat similar, showing that the change of the curvature is not playing a determinant role in the sputtering. Now, we evaluate the role of the erosion in the ripple formation: we quantify the amount of missing atoms in the trough of the ripple, leaving out the crest volume. Using OVITO surface mesh tool [67], we can calculate the induced empty volume under the original surface. We obtain a difference in the solid volume of 4500 atoms between the initial and the final configuration; the total sputtered atoms during the whole simulation was not greater than 1500. More than 3000 atoms need to be included in the sputtering process if we consider that the crest was created by re-deposited atoms. We conclude that, at low incident energy, the erosion can be excluded as a main mechanism of ripple formation. On the other hand, at higher incident energies, the sputtering is stronger and may play more substantial role in pattern formation. Nonetheless, the rippling pattern appear even under negligible sputtering conditions.

In FIGs. 21 b and 21 c, we observe that most of the displacement accumulation takes place at the surface, and it is collected byt those atoms which pile-up on the top of the ripples.

The evolution of δ_z is slow outwards from the surface (positive direction of the z axis) with fluence, in the initially flat and the pre-irradiated surfaces. From the beginning of both simulations, the growth for the initially flat case, additionally, is larger than in the pre-irradiated case. We can observe how the ridge on the pre-irradiated surface mitigates the growth of δ_z. The atoms are displaced in all directions in the created cascades, but the stress relaxation on the surface makes displacements outwards greater. Furthermore, a certain amount of atoms do not receive enough momentum in the direction out to overcome the surface barrier and sputter away, alternatively, these atoms move up and, consequently, they contribute to the positive increase of δ_z. In the case of the pre-existing ridge, the local incidence angle is changed as a result of the ridge influence and, in general, the momentum transferred to the atoms is accumulated in the negative direction of the z-axis, compensating the positive growth of δ_z on the ridge and the remaining flat surface. After about 10000 ions, the initial ridge becomes less pronounced, and the slopes of δ_z for both surfaces evolve similarly.

In FIG. 21 a, we clearly observe that δ_x (parallel to the ion-beam projection) is the largest among all the components, but somewhat lower in the case of the pre-existing ridge surface than in the initially flat surface. We see that the evolution in both cases is rather similar until 20000 impacts. After that moment, they start to differ. Hence, in order to find an explanation for that difference, we pay attention to the evolution of the positive (δ_x^+) and negative (δ_x^-) components independently. The evolution of δ_x^+ with the fluence is similar to the evolution of δ_x since most of the induced momentum is in the positive x-direction. The evolution of δ_x^- with fluence should be different as a result of the reasonably shorter displacements in the negative direction, having a lower accumulation comparing with δ_x^+.

In FIG. 21a, the right y-axis, we plot δ_x^-. In both simulations, the trend of δ_x^- is decreasing

as a function of fluence. In the first stages of the simulations, the cascades do not overlap with the preceding ones, that leads to a pure accumulation of negative displacements. In the case of the pre-irradiated surface we see that this decrease is rather monotonic, on the other hand, for the initially flat surface, the decreasing trend seems to be more puzzling. For the first hundreds Ar impacts, in both cases δ_x^- decreases linearly, because the initially created cascades do not overlap. Both evolve linearly in the negative direction, but in the case of the initially flat surface, this evolution lasts slightly longer. At some point, the trends differ as a consequence of the shape of the surface: the incident ions arrive to the surface with a wider range of angles in the pre-irradiated case, i.e. they can hit the front (forward displacement) and back (backward displacement) slopes of the ridge. The impacts in the back slopes explain the change of the trend, because they scatter away from the surface, due to the grazing incident angle, and they induce backward displacements. This effect is the explanation of the increase in the negative direction of δ_x^-.

The situation changes when the cascades begin to overlap with the previously modified regions. In the initially flat surface, the negative displacement remains almost constant until about 28000 impacts. Since we measure the displacement from the initial atom coordinates, δ_x^- can increase at certain points. After about 27000-30000 Ar^+ impacts, the roughness of the originally flat surface is similar to the pre-irradiated one. At this point we can observe how both curves start to behave similarly, because the effect of the ions over the surface is similar in both cases.

In addition to the analysis performed, the process of the ripple formation observed in the simulations depends on the path that the surface atoms took. We observe that the atomic motion corresponds to biased random movement induced by the incoming ions, depending on the ion impact. In other words, the atom migration is due to a biased surface diffusion, nonetheless the thermal diffusion at room temperature is far from being captured by classical MD simulations used in this work. This effect is explained in FIG. 22.

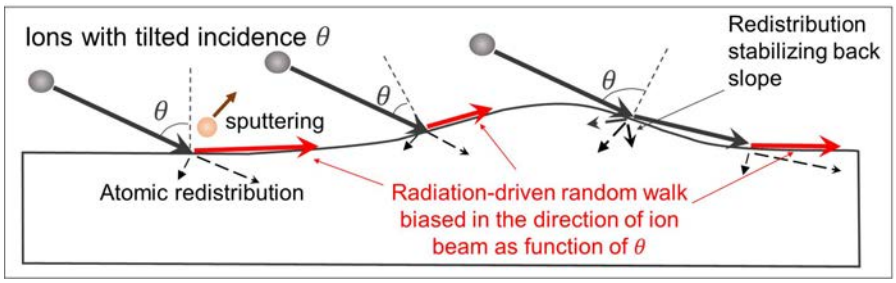

Figure 22: Schematic illustration of the biased surface diffusion induced by ion beam after the initial random roughening of the surface. From [Publication III].

The momentum induced by irradiation depends strongly on the part of the hill where the ion hits. If the ion hits on the front of the hill, it will contribute more to the hill movement

than it it does on the back slope. We observed from the evolution of the surfaces that we can distinguish between two regimes: first, there is a random roughening induced by the ion impacts, as was mentioned before, and those build-up hills are more likely to be moved by irradiation; and second, a formation of the ripples as a consequence of the final ion-induced meeting of the previously created hills. And, at this point, it is more difficult to displace a larger formation. This effect can be observed in FIG. 23 a and b.

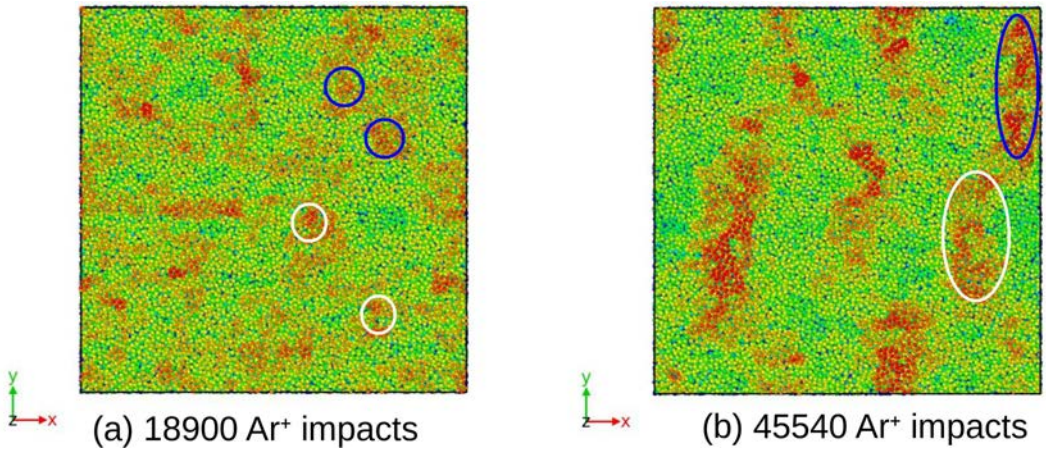

Figure 23: ((a) Several initial hills (colored circles) that eventually meet in a final ridge (b). From [Publication III].

As we can observe from the FIG. 23, the different kinds of events make the early-created hills to merge into a larger ripple. In the case of the pre-existing ridge simulation, that initial modification of the surface enhances the faster formation of new ripples.

This behavior has been shown previously at higher energies [83] related to other effects such as erosion, but in this case erosion cannot be a reason of this change due to the low value of the sputtering, so it has to be related to redistribution. The established theories [30–33, 96, 97] do not predict this effect as a consequence of the redistribution. Hence, these results open the gate for a new understanding of the pattern formation, especially at very low energy. We collected the information about the stress accumulation, but in this case, we did not find any clear correlation of the stress as a function of the fluence with the surface modification.

We emphasize that this was the first time that direct observation and propagation of the surface re-organization was observed using MD. Moreover, we can measure the velocity of propagation of the single-ridge created in the pre-irradiated surface.

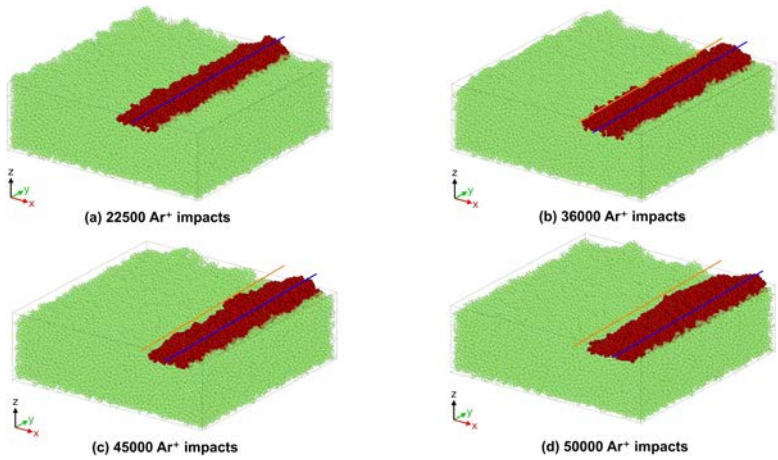

Figure 24: Evolution of the top-most part of the cell under random impact 30 eV-Ar^+ at $\theta = 70°$. The blue line across the cell marks the average position of the crest in that step. The orange line represents the average position in the (a) picture. From [Publication III].

In FIG. 24 we can see how the peak is moving along the x-direction, and we can measure the velocity of the created ridge. Hofsäss et al. [70] measure the velocity of propagation of the ripples created using 10 keV-Xe^+ ions at different irradiation angles, but we will focus on the 70° case, corresponding to a velocity of ≈ 3 nm $/(10^{15}$ Ar^+ $cm^{-2})$. Experimentally, the velocity is measured following one of the ripple peaks at different stages of the irradiation. We propose a similar way to measure it in our case: we choose a step in the simulation where the ripple crest to follow preserves its final form, which is $\sim$ 22500 Ar^+ impacts (8.21×10^{15} Ar^+ cm^{-2}). The velocity is calculated as the evolution of the average position in the x-direction of the peak. Proceeding in this way, we will be able to determine the displacement of the peak as a function of the fluence. The value obtained is 0.27 nm $/(10^{15}$ Ar^+ $cm^{-2})$. We observe that the ripple propagation is a direct consequence of the atomic redistribution induced by the atomic cascades. It is natural to expect a faster propagation of the ripples at irradiation by ions in the keV range than for 30 eV.

The explanation of ripples formation described in this section, in spite of the difference in length scale, shows an analogy of the ion-induced ripple formation with the macroscopic ripples on water or sand. Even though there are many mechanisms which may induce the macroscopic re-organization of the surface in ripples, the principal factors causing these ripples are related to material redistribution as a consequence of an external driving force [98]. This is in apparent agreement with the results for an ion-induced driving force in diffusion-like flow and pile-up effects shown here.

9 SUMMARY

In this dissertation we addressed the possible mechanisms of nanoripple formation by using classical and *speed-up* MD techniques. We have described different methods and results regarding the prediction, simulation and analysis of the ion-induced nano-patterning effect.

In the first place, we described the development of a new technique to obtain a relaxed cell which was used to predict the formation and wavelength of nano-ripples on a-Si under Ar irradiation. The new cell allowed to reach good agreement with experiments. Our results showed a clear difference between MD and BCA for parameterizing the analysis tool for prediction of ripple features such as the wavelength. This was a clear improvement compared to the previous work, where the background displacement, which takes place in an amorphous Si, was to be removed in order to obtain the results. The development of this cell allowed us to study the higher energy irradiation without the background removal as compared to the previous work.

Then, in light of experimental results of nano-pattern formation at ultra-low energy ion irradiation, we developed a *linearly focused mode* for sequential irradiation simulation in order to observe the possible modification of the surface profile at that energy, alongside with the single ion irradiation, which allowed us to predict successfully the wavelength of the formed structures. At that low irradiation energy (30 eV), it was possible to use a much smaller cell, since the low energy ions cause only small displacements. Moreover, the use of the small cell for the single-impact simulations provided reasonably good results compared to the experimental one. The *linearly focused mode* allowed us to analyze the cumulative effect of atomic displacement versus sputtering in sequential irradiation. The eventual surface modification, when experimentally observed, provided more information to the picture of the processes behind the pattern formation at low energy.

Moreover, the same *linearly focused mode* permitted us to determine the difference in the pattern formation in different types of materials: c-Al and a-Si. For doing that, a c-Al cell, comparable in size with the previously developed a-Si, was relaxed. The main goal of this study was to study the differences between the two materials under Ar irradiation. The study lead us to realize that, at low energy, redistribution is the driving force for pattern formation, and the erosion is only a minor factor for the pattern formation in a-Si. For c-Al, at low energy no change of the surface was obtained. Based on our results, we concluded that the atomic redistribution plays a determinant role at low-medium energy in a-Si. However, while erosion is the main driving force in c-Al at medium energy, in the case of the 1000 eV, we observe that the erosion starts playing a more substantial role in both materials. Additionally, we also measure a clear difference between the induced displacements in the two materials, under the same circumstances; in a-Si the displacements are mainly small and, in the case of c-Al, they are well defined at the sequential nearest neighbor distances.

Finally, the application of the *speed-up mode* to the already-proven pattern formation at 30 eV Ar^+ on a-Si, allowed us to observe for the first time using MD the pattern formation

directly. We observed in two different cells, initially flat and with a pre-existing ridge, that the sputtering does not determine the eventual pattern formation and propagation of ripples. The pre-existing ridge clearly accelerates the process of the ripple creation. We could differentiate two regimes in the ripple formation: first, a few separate pileups in the shape of small mounds, where the atoms in the surface re-arrange forming "island-like" structures, and then, these structures merge in larger ridges which build the final ripples.

In general, this work sheds light on the understanding of the pattern formation and the use of computational methods for the study of these phenomena. The simulation approaches developed in this dissertation open up new ways to examine ripple formation theoretically.

Acknowledgements

I wish to thank the former head of the Department of Physics at the University of Helsinki, Prof. Juhani Keinonen, and the current head, Prof. Hannu Koskinen, as well as the head of the Accelerator Laboratory, Prof. Jyrki Räisänen, for providing the facilities for the research presented in this thesis.

I have no words to express my gratitude to my supervisor Prof. Kai Nordlund for all the support, guidance and giving me the opportunity of being part of the group. His positive attitude and dedication have been of great help. I wish to express my gratitude to my co-supervisor Prof. Flyura Djurabekova, your patience, determination and knowledge have been lessons to me. I will be eternally thankful.

I thank all my colleagues at the Accelerator Laboratory for all the good moments that we have shared. Specially, I want to thank Junlei for his friendship and all the support. Thank you, Andreas, for the long and interesting conversations in which our valuable friendship is based on. I wish to thank Laura for the help and support since my first step into the lab. Thank you, Andrey, for all the patience and dedication, I have learned a lot from you.

I wish to express my gratitude to Prof. Michael Aziz, Dr. Joy Perkinson and, specially, Prof. Scott Norris for the advice and fruitful discussions during our collaboration, besides of being a great host in Dallas. I want to thank Dr. Debasree Chowdhury for the interesting conversations and dedication to our work together.

I also want to thank Daniel for all the advice and support provided, specially during my first year in Finland. I wish to express my gratitude to the Pérez Arenas family, and specially Lucía, you encouraged me to take the decision of coming to Finland. I will be eternally grateful. Moreover, I want to use these lines to thank Alvaro, Jose and Aroa for their unconditional friendship and all the good moments. Thank you, Ramon, for making my stay in Finland easier and becoming one of my best friends. I also want to thank Tiago, Marta, Hilal, Kaisa and Sabine for all the good memories.

I thank Oskar for always being there for me and my family. I would also like to thank my friends in Cordoba, you are the Andalusian meaning of *Sisu*. Thank you, Gabriel, for our unforgettable trips around Europe and, specially, Antonio and Marina, for all the support and the reminder that the family goes beyond the blood.

Most of all I want to thank Alba, for being such an amazing person. Your unconditional love and understanding at home make my day. Your smile is the best gift that I could receive. I love you.

Finally, I want to thank my family. My uncle, aunts and cousin, for be there whenever my parents needed it, I will never forget that. My sister, your constant and huge love is a cornerstone of my well-being. The distance makes me miss you even more I want to admit. My father, he has been always there for me whatever I needed and his advice, dedication, support and critical thinking are the most precious things that a son can receive, you are a model for me. My mother, the bravest person in my life, her tenacity,

wisdom and profound sense of duty are what I admire the most. Without your guidance and love, I would never have achieved anything.

Helsinki, August 29th, 2019

Alvaro Lopez Cazalilla

References

[1] "Why do regular, wavelike shapes form when the wind blows over the sand on the beach for a long time? and what determines the spacing (frequency) of these waves?" https://www.scientificamerican.com/article/why-do-regular-wavelike-s/, accessed: 2018-08-08.

[2] O. Terzidis, P. Claudin, and J.-P. Bouchaud, "A model for ripple instabilities in granular media," *Eur. Phys. J. B*, vol. 5, p. 245, 1998.

[3] A. Valance and F. Rioual, "A nonlinear model for aeolian sand ripples," *Eur. Phys. J. B*, vol. 10, p. 543, 1999.

[4] Z. Csahók, C. Misbah, F. Rioual, and A. Valance, "Dynamics of aeolian sand ripples," *Eur. Phys. J. E*, vol. 3, p. 71, 2000.

[5] W. L. Chan and E. Chason, "Making waves: Kinetic processes controlling surface evolution during low energy ion sputtering," *J. Appl. Phys.*, vol. 101, p. 121301, 2007.

[6] S. Facsko, T. Dekorsy, C. Koerdt, C. Trappe, H. Kurz, A. Vogt, and H. Hartnagel, "Formation of ordered nanoscale semiconductor dots by ion sputtering," *Science*, vol. 285, p. 1551–1553, 1999.

[7] B. Ziberi, F. Frost, T. Höche, and B. Rauschenbach, "Ripple pattern formation on silicon surfaces by low-energy ion-beam erosion: experiment and theory," *Phys. Rev. B*, vol. 72, p. 235310, 2005.

[8] U. Valbusa, C. Boragno, and F. Buatier de Mongeot, "Nanostructuring surfaces by ion sputtering," *J. Phys.: Condens. Matter*, vol. 14, p. 8153, 2002.

[9] A. Cuenat, H. George, K.-C. Chang, J. Blakely, and M. Aziz, "Lateral templating for guided self-organization of sputter morphologies," *Adv. Mater.*, vol. 17, pp. 2845–2849, 2005.

[10] C. S. Madi, H. B. George, and M. J. Aziz, "Linear stability and instability patterns in ion-sputtered silicon," *J. Phys. Condes. Matt.*, vol. 21, p. 224010, 2009.

[11] A. Lopez-Cazalilla, D. Chowdhury, A. Ilinov, S. Mondal, P. Barman, S. R. Bhattacharyya, D. Ghose, F. Djurabekova, K. Nordlund, and S. Norris, "Pattern formation on ion-irradiated Si surface at energies where sputtering is negligible," *J. Appl. Phys.*, vol. 123, p. 235108, 2018.

[12] C. S. Madi and M. J. Aziz, "Multiple scattering causes the low energy–low angle constant wavelength topographical instability of argon ion bombarded silicon surfaces," *Appl. Surf. Sci.*, vol. 258, pp. 4112–4115, 2012.

[13] R. L. Cunningham, P. Haymann, C. Lecomte, W. J. Moore, and J. J. Trillat, "Etching of surfaces with 8-keV argon ions," *J. Appl. Phys.*, vol. 31, p. 839, 1960.

[14] Navez, M. and Sella, C. and Chaperot, D., "Etude de le attaque du verre par bombardement ionique," *Comptes Rendus Acad. Sci. Paris*, vol. 254, p. 240, 1962.

[15] P. Sigmund, "A mechanism of surface micro-roughening by ion bombardment," *J. Mater. Sci.*, vol. 8, p. 1545, 1973.

[16] R. M. Bradley and J. M. Harper, "Theory of ripple topography induced by ion bombardment," *J. Vac. Sci. Technol.*, vol. 6, p. 2390–2395, 1988.

[17] G. Carter and V. Vishnyakov, "Roughening and ripple instabilities on ion-bombarded Si," *Phys. Rev. B*, vol. 54, pp. 17 647–53, 1996.

[18] B. Davidovitch, M. Aziz, and M. Brenner, "On the stabilization of ion sputtered surfaces," *Phys. Rev. B*, vol. 76, p. 205420, 2007.

[19] S. A. Norris, M. P. Brenner, and M. J. Aziz, "From crater functions to partial differential equations: a new approach to ion bombardment induced nonequilibrium pattern formation," *Journal of Physics: Condensed Matter*, vol. 21, no. 22, p. 224017, 2009.

[20] S. A. Norris, J. Samela, C. S. Madi, M. P. Brenner, L. Bukonte, M. Backman, F. Djurabekova, K. Nordlund, and M. J. Aziz, "MD-Predicted phase diagrams for pattern formation," *Nature Communications*, vol. 2, p. 276, 2011.

[21] A. Lopez-Cazalilla, A. Ilinov, L. Bukonte, F. Djurabekova, K. Nordlund, S. Norris, and J. Perkinson, "Simulation of atomic redistribution effects in a-Si under ion irradiation," *Nucl. Instr. Meth. Phys. Res. B*, vol. 414, pp. 133–140, 2018.

[22] M. Koster and H. Urbassek, "Modification of a-Si under 100 eV Si atom bombardment," *Nucl. Instr. and Meth. in Phys. Res. B*, vol. 180, pp. 299–305, 2001.

[23] S. A. Norris, "Stability analysis of a viscoelastic model for ion-irradiated silicon," *Phys. Rev. B*, vol. 85, p. 155325, 2012.

[24] S. A. Norris, "Stress-induced patterns in ion-irradiated silicon: Model based on anisotropic plastic flow," *Phys. Rev. B*, vol. 86, p. 235405, 2012.

[25] A. Moreno-Barrado, M. Castro, R. Gago, L. Vazquez, J. Muñoz-Garcia, A. Redondo-Cubero, B. Galiana, C. Ballesteros, and R. Cuerno, "Nonuniversality due to inhomogeneous stress in semiconductor surface nanopatterning by low-energy ion-beam irradiation," *Phys. Rev. B*, vol. 91, p. 155303, 2015.

[26] A. Lopez-Cazalilla, A. Ilinov, F. Djurabekova, and K. Nordlund, "Modeling of high-fluence irradiation of amorphous Si and crystalline Al by linearly focused Ar ions," *J. Phys.: Condens. Matter*, vol. 31, p. 075302, 2019.

[27] A. Lopez-Cazalilla, A. Ilinov, C. Fridlund, F. Djurabekova, and K. Nordlund, "Nonlinear effects during formation and propagation of ion-induced surface ripples," *under revision in Science Advances*, vol. 1, p. 1, 2019.

[28] C. Fridlund, J. Laakso, K. Nordlund, and F. Djurabekova, "Atomistic simulation of ion irradiation of semiconductor heterostructure," *Nucl. Instr. Meth. Phys. Res. B*, vol. 409, p. 14, 2017.

[29] P. Sigmund, "Theory of Sputtering. I. Sputtering Yield of Amorphous and Polycrystalline Targets," *Phys. Rev.*, vol. 184, p. 383, 1969.

[30] R. Cuerno and A.-L. Barabasi, "Dynamic scaling of ion-sputtered surfaces," *Phys. Rev. Lett.*, vol. 74, p. 4746, 1995.

[31] M. Makeev and A.-L. Barabasi, "Ion-induced effective surface diffusion in ion sputtering," *Appl. Phys. Lett.*, vol. 71, p. 2800, 1997.

[32] M. Makeev, R. Cuerno, and A.-L. Barabasi, "Morphology of ion-sputtered surfaces," *Nucl. Instr. and Meth. in Phys. Res. B*, vol. 197, p. 185–227, 2002.

[33] M. Makeev and A.-L. Barabasi, "Effect of surface morphology on the sputtering yields. I. Ion sputtering from self-affine surfaces," *Nucl. Instr. and Meth. in Phys. Res. B*, vol. 222, pp. 316–334, 2004.

[34] M. Kardar, G. Parisi, and Y.-C. Zhang, "Dynamic scaling of growing interfaces," *Phys. Rev. Lett.*, vol. 56, p. 9, 1986.

[35] E. Chason, T. M. Mayer, B. K. Kellerman, D. T. McIlroy, and A. J. Howard, "Roughening Instability and Evolution of the Ge(001) Surface during Ion Sputtering," *Phys. Rev. Lett.*, vol. 72, p. 19, 1994.

[36] N. Kalyanasundaram, M. Ghazisaeidi, J. B. Freund, and H. T. Johnson, "Single impact crater functions for ion bombardment of silicon," *Appl. Phys. Lett.*, vol. 92, p. 131909, 2008.

[37] M. Moore, N. Kalyanasundaram, J. B. Freund, and H. T. Johnson, "Structural and sputtering effects of medium energy ion bombardment of silicon," *Nucl. Instr. Meth. Phys. Res. B*, vol. 225, pp. 241–255, 2004.

[38] M. Harrison and R. Bradley, "Crater function approach to ion-induced nanoscale pattern formation: Craters for surfaces are insufficient," *Phys. Rev. B*, vol. 89, p. 245401, 2014.

[39] S. A. Norris, "Pycraters: A python framework for the collection of crater function statistics." *arXiv:1410.8489*.

[40] E. Anzenberg, C. S. Madi, M. J. Aziz, and K. Ludwig Jr., "Time-resolved measurements of nanoscale surface pattern formation kinetics in two dimensions on ion-irradiated Si," *Phys. Rev. B*, vol. 84, p. 214108, 2011.

[41] C. S. Madi, E. Anzenberg, K. Ludwig Jr., and M. J. Aziz, "Mass redistribution causes the structural richness of ion-irradiated surfaces," *Phys. Rev. Lett.*, vol. 106, p. 066101, 2011.

[42] M. Teichmann, J. Lorbeer, B. Ziberi, F. Frost, and B. Rauschenbach, "Pattern formation on Ge by low energy ion beam erosion," *New J. Phys.*, vol. 15, p. 103029, 2013.

[43] J. C. Perkinson, E. Anzenberg, M. J. Aziz, and K. F. J. Ludwig, "Model-independent test of the truncated crater function theory of surface morphology evolution during ion bombardment," *Phys. Rev. B*, vol. 89, p. 115433, 2014.

[44] H. Hofsäss, "Surface instability and pattern formation by ion-induced erosion and mass redistribution," *Appl. Phys. A*, vol. 114, pp. 401–422, 2014.

[45] B. Alder and T. Wainwrite, "Phase transition for a hard sphere system," *J. of Chem. Phys.*, vol. 27, p. 1208, 1957.

[46] J. Gibson, A. Goland, and M. M. G. Vineyard, "Dynamics of radiation damage," *Phys. Rev.*, vol. 120, p. 1229, 1960.

[47] L. Verlet, "Computer 'Experiments' on Classical Fluids. I. Thermodynamical Properties of Lennard-Jones Molecules," *Phys. Rev.*, vol. 159, p. 98, 1967.

[48] L. Verlet, "Computer 'Experiments' on Classical Fluids. II. Equilibrium Correlation Functions," *Phys. Rev.*, vol. 165, p. 201, 1967.

[49] C. Gear, *Numerical Initial Value Problems in Ordinary Differential Equations.* Upper Saddle River, NJ, USA: Prentice Hall PTR, 1971.

[50] K. Nordlund, 2010, PARCAS computer code. The main principles of the molecular dynamics algorithms are presented in [**?** **?**]. The adaptive time step and electronic stopping algorithms are the same as in [56].

[51] H. J. C. Berendsen, J. P. M. Postma, W. F. van Gunsteren, A. DiNola, and J. R. Haak, "Molecular dynamics with coupling to external bath," *J. Chem. Phys.*, vol. 81, no. 8, p. 3684, 1984.

[52] S. Nosé, "A unified formulation of the constant temperature molecular dynamics methods," *J. Chem. Phys.*, vol. 81, p. 511, 1984.

[53] K. Nordlund, "Energy loss of energetic ions," http://beam.helsinki.fi/~knordlun/mdh/rangetext.html, accessed: 2018-08-30.

[54] M. Robinson and I. Torrens, "Computer simulation of atomic-displacement cascades in solids in the binary-collision approximation," *Phys. Rev. B*, vol. 9, p. 5008, 1974.

[55] J. F. Ziegler, J. P. Biersack, and U. Littmark, "The stopping and range of ions in matter," *(Pergamon, New York)*, 1985.

[56] K. Nordlund, "Molecular dynamics simulation of ion ranges in the 1 – 100 keV energy range," *Comput. Mater. Sci.*, vol. 3, p. 448, 1995.

[57] M. Z. Bazant, E. Kaxiras, and J. F. Justo, "Environment dependent interatomic potential for bulk silicon," *Phys. Rev. B*, vol. 56, p. 8542, 1997.

[58] J. F. Justo, M. Z. Bazant, E. Kaxiras, V. V. Bulatov, and S. Yip, "Interatomic potential for silicon defects and disordered phases," *Phys. Rev. B*, vol. 58, p. 2539, 1998.

[59] K. Nordlund, N. Runeberg, and D. Sundholm, "Repulsive interatomic potentials calculated using hartree-fock and density-functional theory methods," *Nucl. Instr. Meth. Phys. Res. B*, vol. 132, pp. 45–54, 1997.

[60] J. Nord, K. Nordlund, and J. Keinonen, "Amorphization mechanism and defect structures in ion beam amorphized Si, Ge and GaAs," *Phys. Rev. B*, vol. 65, p. 165329, 2002.

[61] M. S. Daw, S. M. Foiles, and M. I. Baskes, "The embedded-atom method: a review of theory and applications," *Mat. Sci. Rep.*, vol. 9, p. 251, 1993.

[62] F. Ercolessi and J. B. Adams, "Interatomic Potentials from First-Principles Calculations: the Force-Matching Method," *Europhys. Lett.*, vol. 26, p. 583, 1994.

[63] K. Nordlund, M. Ghaly, and R. S. Averback, "Mechanisms of ion beam mixing in metals and semiconductors," *J. Appl. Phys.*, vol. 83, no. 3, pp. 1238–1246, 1998.

[64] F. Wooten, K. Winer, and D. Weaire, "Computer Generation of Structural Models of Amorphous Si and Ge," *Phys. Rev. Lett.*, vol. 54, p. 1392, 1985.

[65] L. Bukonte, F. Djurabekova, J. Samela, K. Nordlund, S. A. Norris, and M. J. Aziz, "Comparison of molecular dynamics and binary collision approximation simulations for atom displacement analysis," *Nucl. Instr. Meth. Phys. Res. B*, vol. 297, pp. 23–28, 2013.

[66] F. Frost, R. Fechner, B. Ziberi, J. Völlner, D. Flamm, and A. Schindler, "Large area smoothing of surfaces by ion bombardment: fundamentals and applications," *J. Phys.: Condens. Matter*, vol. 21, p. 224026, 2009.

[67] A. Stukowski, *JOM*, vol. 66, p. 399, 2014.

[68] P. Süle and K. H. Heinig, "The molecular dynamics simulation of ion-induced ripple growth," *The Journal of Chemical Physics*, vol. 131, p. 204704, 2009.

[69] E. O. Yewande, R. Kree, and A. K. Hartmann, "Numerical analysis of quantum dots on off-normal incidence ion sputtered surfaces," *Phys. Rev. B*, vol. 75, p. 155325, 2007.

[70] H. Hofsäss, K. Zhang, H. G. Gehrke, , and C. Brüsewitz, "Propagation of ripple patterns on Si during ion bombardment," *Phys. Rev. B*, vol. 88, p. 075426, 2013.

[71] M. Robinson, "Computer simulation studies of high-energy collsion cascades," *Nucl. Instr. Meth. Phys. Res. B: Beam Interactions with Materials and Atoms*, vol. 67, p. 396, 1992.

[72] F. Djurabekova, F. Umarov, and S. Yugay, *IEEE*, vol. 228, p. 066101, 2000.

[73] G. Ozaydin, A. S. Özcan, Y. Wang, K. Ludwig, H. Zhou, R. Headrick, and D. Siddons, "Real-time x-ray studies of Mo-seeded Si nanodot formation during ion bombardment," *Appl. Phys. Lett.*, vol. 87, p. 163104, 2005.

[74] D. Chowdhury, D. Ghose, and S. Mollick, "Homoepitaxy of germanium by hyperthermal ion irradiation," *Vacuum*, vol. 179, pp. 23–27, 2014.

[75] D. Chowdhury, D. Ghose, and B. Satpati, "Production of ordered and pure Si nanodots at grazing ion beam sputtering under concurrent substrate rotation," *Materials Science and Engineering: B*, vol. 179, pp. 1–5, 2014.

[76] E. Anzenberg, J. Perkinson, C. S. Madi, M. J. Aziz, and K. Ludwig Jr., "Nanoscale surface pattern formation kinetics on germanium irradiated by Kr^+ ions," *Phys. Rev. B*, vol. 86, p. 245412, 2012.

[77] T. Kyuno, D. Cahill, R. Averback, J. Tarus, and K. Nordlund, "Surface Defects and Bulk Defect Migration Produced by Ion Bombardment of Si(001)," *Phys. Rev. Lett.*, vol. 83, p. 23, 1999.

[78] C. S. Madi, B. Davidovitch, H. B. George, S. Norris, M. Brenner, and M. J. Aziz, "Multiple bifurcation types and the linear dynamics of ion sputtered surfaces," *Phys. Rev. Lett.*, vol. 101, p. 246102, 2008.

[79] P. Bedrossian, "Generation and healing of low-energy ion-induced defects on Si(100)-2x1," *Surf. Sci.*, vol. 301, pp. 223–232, 1994.

[80] S. MacLaren, J. Baker, N. Finnegan, and C. Loxton, "Surface-roughness development during sputtering of GaAs and InP - evidence for the role of surface-diffusion in ripple formation and sputter cone development," *J. Vac. Sci. Technol. A*, vol. 10, p. 468, 1992.

[81] H. Feil, H. Zandvliet, M.-H. Tsai, J. Dow, and I. Tsong, "Random and Ordered Defects on Ion-Bombarded Si(100)-(2x1) Surfaces," *Phys. Rev. Lett.*, vol. 69, p. 21, 1992.

[82] P. Karmakar and D. Ghose, "Ion beam sputtering induced ripple formation in thin metal films," *Surf. Sci.*, vol. 554, p. L101, 2004.

[83] M. Castro, R. Gago, L. Vazquez, J. Muñoz-Garcia, and R. Cuerno, "Stress-induced solid flow drives surface nanopatterning of silicon by ion-beam irradiation," *Phys. Rev. B*, vol. 86, p. 214107, 2012.

[84] A.-D. Brown and J. Erlebacher, "Temperature and fluence effects on the evolution of regular surface morphologies on ion-sputtered Si (111)," *Phys. Rev. B*, vol. 72, p. 075350, 2005.

[85] K. Smith and C. Oatley, "The scanning electron microscope and its fields of application," *J. Appl. Phys.*, vol. 6, p. 391, 1955.

[86] "Scanning electron microscopy 1928-1965," http://www-g.eng.cam.ac.uk/125/achievements/mcmullan/mcm.htm, accessed: 2018-12-05.

[87] "Scanning electron microscopy," https://www.nanoscience.com/techniques/scanning-electron-microscopy/, accessed: 2018-10-8.

[88] O.-P. Choudhary and Priyanka, "Scanning electron microscope: Advantages and disadvantages in imaging components," *Int. J. Curr. Microbiol. App. Sci.*, vol. 6, pp. 1877–1882, 2017.

[89] B. Smith, "The differences between atomic force microscopy and scanning electron microscopy," https://www.azom.com/article.aspx?ArticleID=11879, accessed: 2018-10-23.

[90] S. Habenicht, K. Lieb, J. Koch, and A. Wieck, "Ripple propagation and velocity dispersion on ion-beam-eroded silicon surfaces," *Phys. Rev. B*, vol. 65, p. 115327, 2002.

[91] J. Zhou, M. Hildebrandt, and M. Lu, "Self-organized antireflecting nano-cone arrays on Si (100) induced by ion bombardment," *J. Appl. Phys*, vol. 109, p. 053513, 2011.

[92] G. Binnig, C. F. Quate, and C. Gerber, "Atomic force microscopy," *Phys. Rev. Lett.*, vol. 56, p. 9, 1986.

[93] L. Gross, F. Mohn, N. Moll, P. Liljeroth, and G. Meyer, "The chemical structure of a molecule resolved by atomic force microscopy," *Science*, vol. 325, pp. 1110–1114, 2009.

[94] F.-J. Giessibl, "Advances in atomic force microscopy," *Reviews of Modern Physics*, vol. 75, p. 949, 2003.

[95] "The Common AFM Modes," http://www.chembio.uoguelph.ca/educmat/chm729/afm/details.htm, accessed: 2018-12-05.

[96] M. Castro, R. Cuerno, L. Vazquez, and R. Gago, "Self-organized ordering of nanostructures produced by ion-beam sputtering," *Phys. Rev. Lett.*, vol. 94, p. 016102, 2005.

[97] J. Muñoz-Garcia, M. Castro, and R. Cuerno, "Nonlinear ripple dynamics on amorphous surfaces patterned by ion beam sputtering," *Phys. Rev. Lett.*, vol. 96, p. 086101, 2006.

[98] A. Fourriere, P. Claudin, and B. Andreotti, "Bedforms in a turbulent stream: formation of ripples by primary linear instability and of dunes by nonlinear pattern coarsening," *Journal of fluid mechanics*, vol. 649, pp. 287–328, 2010.